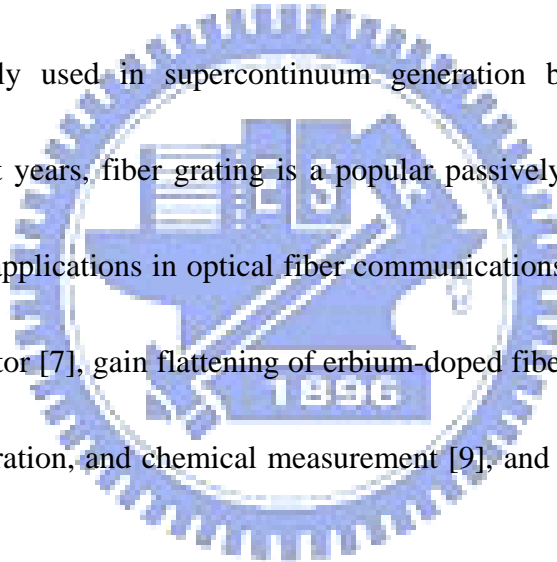


# Chapter 1 Introduction

## 1.1 Significance of this thesis

The spectral broadening of a coherent or partially coherent light signal in optical fibers has captured much attention in recent years, fuelled by using photonic crystal fibers (PCFs) presenting very high nonlinear response [1]. The phenomenon is called supercontinuum (SC), which is a low-cost ultra-wideband light sources and has many practical applications in optical communications [2-3], optical frequency metrology [4], and sensor technology [5-6].

PCFs are not only used in supercontinuum generation but also made as optical components. In recent years, fiber grating is a popular passively components, which have found a wide range of applications in optical fiber communications and sensing system, such as dispersion compensator [7], gain flattening of erbium-doped fiber amplifiers [8], sensor for temperature, strain, vibration, and chemical measurement [9], and band rejection filters [10], etc.



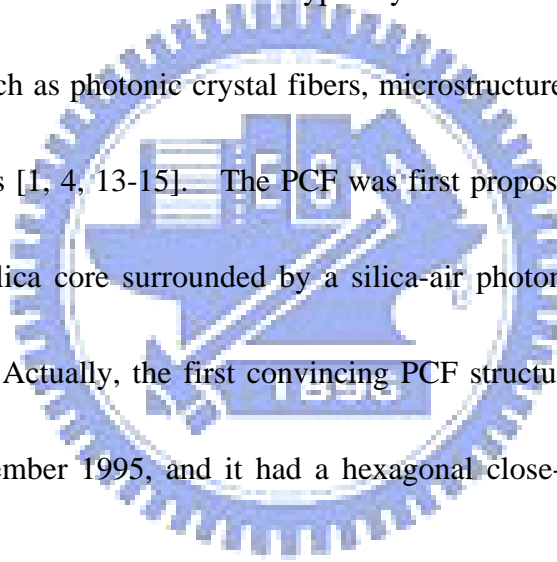
## 1.2 Background

### 1.2.1 What are photonic crystal fibers

Photonic crystal fibers are novel optical waveguides that usually composed of a single material (typically silica) with multiple air-holes periodically arranged around the core that run along the length of the cladding. The cross section of PCF consists of a two-dimensional periodic structure, where the periodicity is broken by the presence of a central defect.

Introducing a defect or a missing hole at the center of the fiber forms the core of PCF.

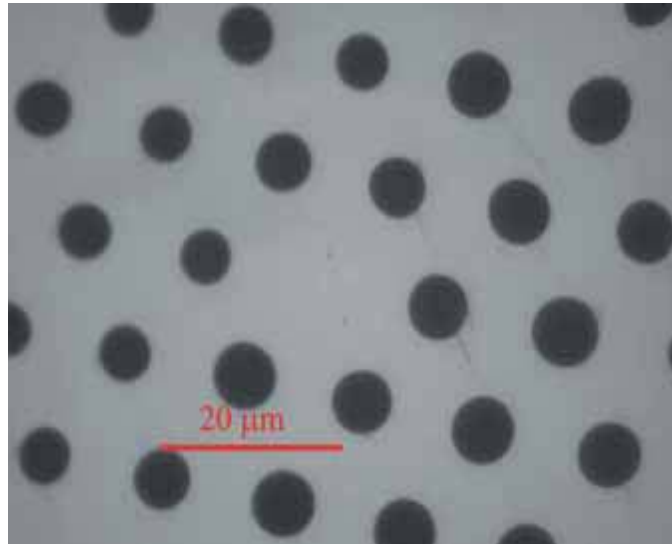
The concept of photonic crystal fiber is due to photonic crystal dating back to 1987, when it was suggested by Eli Yablonovitch [11] and Sajeev John [12] that the electronic bandgaps of semiconductors had an optical analogy in periodic dielectric structures. This suggestion initiated research activities in the following years and finally lead to the birth of a new class of optical fibers, in which the cladding structure consists of a periodic system of air-holes in a matrix of dielectric material – typically silica. These new fibers have been given several names such as photonic crystal fibers, microstructured fibers, holey fibers, and photonic bandgap fibers [1, 4, 13-15]. The PCF was first proposed and fabricated in 1996. It consists of a pure silica core surrounded by a silica-air photonic crystal material with a hexagonal symmetry. Actually, the first convincing PCF structure emerged from the fiber drawing tower in November 1995, and it had a hexagonal close-packed array of small air channels.



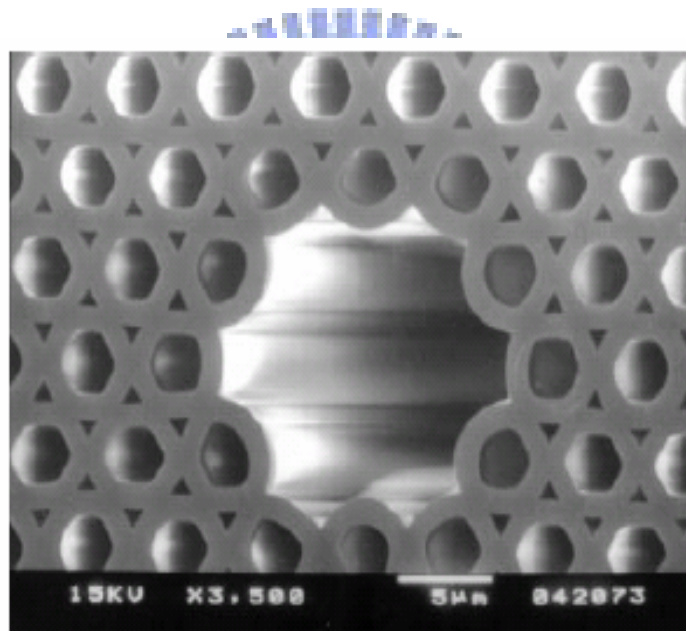
In general, PCFs can be divided into two classes according to the light confinement mechanism: (1) the index guiding effect, also called modified total internal reflection (TIR) (microstructured fiber, MF), and (2) the photonic bandgap (PBG) effect (photonic bandgap fiber, PBF). Fig. 1.1(a) shows the MF whose solid core is surrounded by an array of air holes, in which the confinement mechanism is similar to that of conventional fibers. Due to its higher refractive index of the core than cladding, the optical field is trapped around a

high-index core and light is guided by the principle of total internal reflection. Conversely, the PBFs are fibers which guide light in their hollow core. Fig. 1.1(b) shows the scheme of a PBF. In PBFs, the periodic arrangement of the air holes can be considered as the photonic bandgap structure and their hollow core is the defect inside the structure. The photonic bandgaps structure will result in bandgap which allows only certain range of wavelength existing in it. Outside the range, PBFs is anti-guiding.





(a)



(b)

Fig. 1.1 Scanning electron microscope image of the end of photonic-crystal-fibers: (a) index-guiding PCF; (b) photonic bandgap fiber.

### 1.2.2 Applications of photonic crystal fibers

Properties of PCFs have been shown strongly dependent on the geometry of the PCF cross section, in particular on the shape, dimension, pitch, and arrangement of the air holes [16]. In comparison with conventional optical fibers, PCFs provide extraordinary dispersion properties [17], endlessly single-mode guidance [16], light guidance in air [18], an order of magnitude higher birefringence [13], and enhanced nonlinear effects [1], etc. These special properties of PCFs have led to the development of several potential applications in a variety of fields, ranging from communication fiber to optoelectronic devices such as couplers [19], attenuators [20], polarization splitters [21], dispersion compensators [22], sensor technology [23], fiber gratings [24], and supercontinuum generation [25], etc.

In this thesis, we study long-period fiber gratings and high pulse energy lasers for supercontinuum generation by using photonic crystal fibers. Because long-period grating can be used as band-rejection filter while supercontinuum is a high coherent white-light source, they can find various applications in optical communication technology.

### 1.2.3 Supercontinuum generation using PCFs

Supercontinuum (SC) generation is the formation of broad continuous spectra by propagation of high power optical pulses through nonlinear media [26]. Provided high-enough power, SC generation can be observed in a drop of water [27]. However, the nonlinear effects involved in the spectral broadening are highly dependent on the dispersion

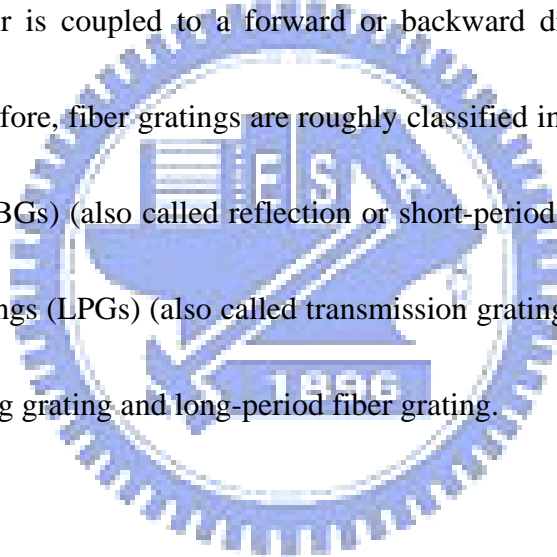
of the media, and a clever dispersion design can significantly reduce the power required. The widest spectra are obtained when the pump pulses are launched close to the zero-dispersion wavelength of the nonlinear media. Due to the technology in fabricating shiftable dispersion profile and small core, MF become powerful component in generating SC and was first demonstrated in 1999 [28]. The zero-dispersion wavelength of MFs can be shifted close to the pump wavelength and the small core of MFs enhances the nonlinear effects; these are mechanisms leading to the SC generation.

To generate the SC with MFs, femtosecond [29] and picosecond mode-locked laser systems were generally used as the pump sources [30]. For femtosecond pumping, it is easy to get higher peak power for the pumping pulse due to its ultrashort pulse duration and thus inducing strong nonlinear effects. These nonlinear effects include high-order soliton breakup [31], self-frequency shift [32] and four-wave mixing [33]. Usually about mini-watts of average pumping power are needed to generate the supercontinuum for a femtosecond mode-locked laser system [29]. However, a femtosecond mode-locked laser system is more expensive and complicated to build. A picosecond mode-locked laser system is a better way. For picosecond pumping, the major nonlinear effects for spectrum broadening are modulation instability and stimulated Raman scattering if the PCF is pumped in the anomalous dispersion region, where the group-velocity dispersion  $\beta_2$  is negative. In 2002, Mickael Seefeldt reported the SC from 700 nm to 1600 nm with an average input power of 5.0 W using

passively mode-locked Nd:YVO<sub>4</sub> which generated a pulse width of 10 ps. Compared with femtosecond pumping, an average power up to several watts would be needed to generate sufficient supercontinuum for picosecond pumping due to its longer duration of pulse width. Therefore, a higher average power is necessary to get enough pumping peak power.

### **1.2.4 Fiber gratings**

When periodic index perturbation is generated in the core region of the fiber, light propagation in the fiber is coupled to a forward or backward direction depending on the grating periods. Therefore, fiber gratings are roughly classified into two types: one is called fiber Bragg gratings (FBGs) (also called reflection or short-period gratings), and the other is called long-period gratings (LPGs) (also called transmission gratings). Now, we will simply introduce the fiber Bragg grating and long-period fiber grating.



#### **1.2.4.1 Fiber Bragg grating**

The devices of fiber Bragg grating (FBG) play a very important role in fiber optic communication systems. The major applications are such as filtering, add/drop multiplexing, gain equalization, laser wavelength stabilization, and dispersion compensation for accumulated dispersion in the system. In this section, the operation principles of fiber Bragg grating will be briefly reviewed.

A fiber grating is a periodic perturbation in the refractive index along the fiber by using

the photosensitivity of certain types of optical fibers. The formation of permanent gratings in an optical fiber was first demonstrated by Hill et. al, in 1987 [34]. They launched intense argon-ion laser radiation into a germanium-doped fiber and observed an increase in the reflected light intensity. Since then, grating-writing technologies such as phase masks have matured to produce gratings. When a phase mask is illuminated by an ultraviolet light beam (248 nm) shown in Figure 1.2, it splits the beams into different  $\pm 1$  diffractive orders, which then interfere with one another to write the grating into the fiber. The fiber gratings we will discuss in this section include uniform and chirped fiber Bragg gratings.

For uniform and chirped FBG, the index perturbation  $\Delta n(z)$  in fiber gratings can be expressed as

$$\Delta n(z) = \Delta n_0(z) \left[ 1 + m \cdot \cos\left(\frac{2\pi}{\Lambda} z\right) \right] \quad (1.1.5-1)$$

Where  $z$  is the position along the grating,  $\Delta n_0(z)$  is the maximum index modulation, and  $m$  is the contrast number (which is determined by the visibility of the UV fringe pattern).

The strongest constructive interaction occurs at the Bragg wavelength  $\lambda_B$ , which is given by

$$\lambda_B = 2n_{\text{eff}}\Lambda \quad (1.1.5-2)$$

Where  $n_{\text{eff}}$  is the effective core index of refraction over a spatial average of  $\Delta n(z)$  and  $\Lambda$  is the uniform grating pitch. Since constructive interference occurs in the back-reflected wave, the grating will only reflect the spectral component that matches (1.1.5-2) but does nothing to the remaining components of the incident light, which provides the filter



characteristic shown in Figure 1.3.

If the grating pitch  $\Lambda(z)$  is not a constant but a monotonically increasing or decreasing function, the grating is called a chirped grating that reflects different wavelengths at different positions along it. The Bragg condition in a chirped grating will then be modified as

$$\lambda_B(z) = 2n_{\text{eff}}(z)\Lambda(z) \quad (1.1.5-3)$$

If  $\lambda_B(z)$  varies linearly as a function of position over the grating, such a grating is called a linearly chirped fiber Bragg grating. With this characteristic, different frequency components of an incident light are reflected at different points, depending on where the Bragg condition is satisfied locally. From Figure 1.4, it is easy to understand the operation of a chirped FBG. For conventional single-mode fiber with positive dispersion at the wavelength of 1.55  $\mu\text{m}$  region, the short-wavelength (high-frequency) components of an optical pulse propagate faster than the long-wavelength (low-frequency) components. The short-wavelength needs to travel further into the grating before being reflected and thus experiences more time delay than long-wavelength components. As a result, the grating induced time delay should be opposite to the fiber dispersion. The grating-induced dispersion  $D_g$  (ps/nm) can be determined by

$$D_g = \frac{\tau_g}{\Delta\lambda} = \frac{2n_{\text{eff}}L_g}{c\Delta\lambda} \quad (1.1.5-4)$$

where  $L_g$  is the length of the FBG,  $\Delta\lambda$  is the Bragg wavelength differential at the two ends of the grating,  $c$  is the speed of light, and  $\tau_g = \frac{2n_{\text{eff}}L_g}{c}$  is the round-trip time inside the grating.

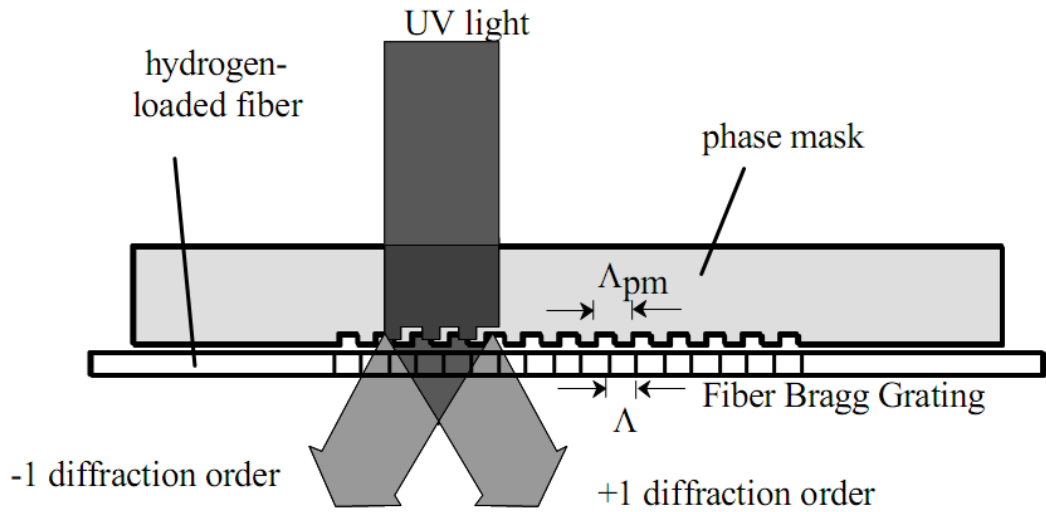


Fig. 1.2 Phase mask technique for writing fiber Bragg grating

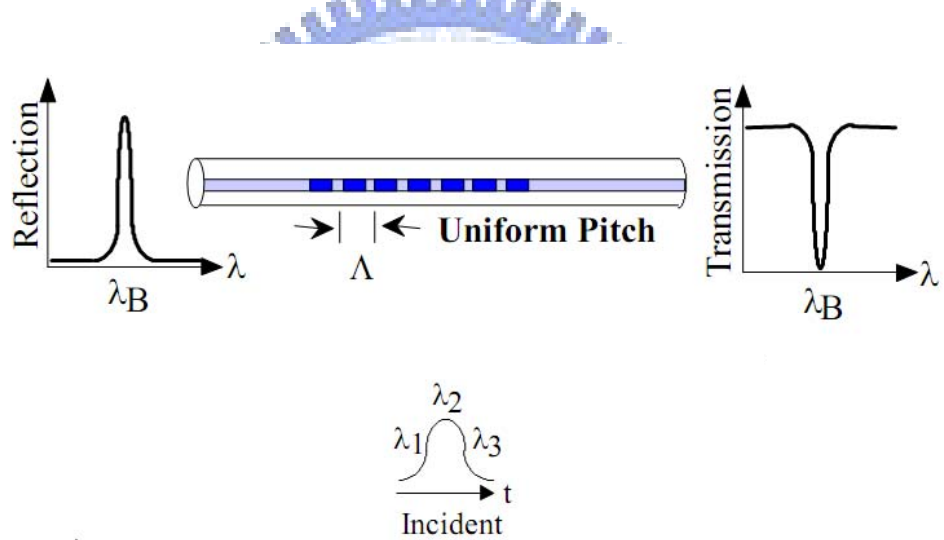


Fig. 1.3 The reflection and transmission spectra of a uniform Bragg grating

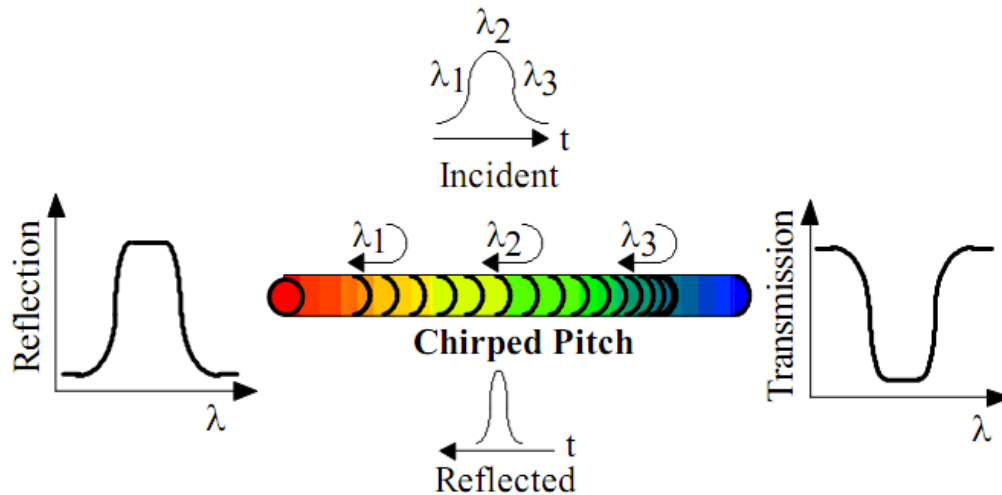


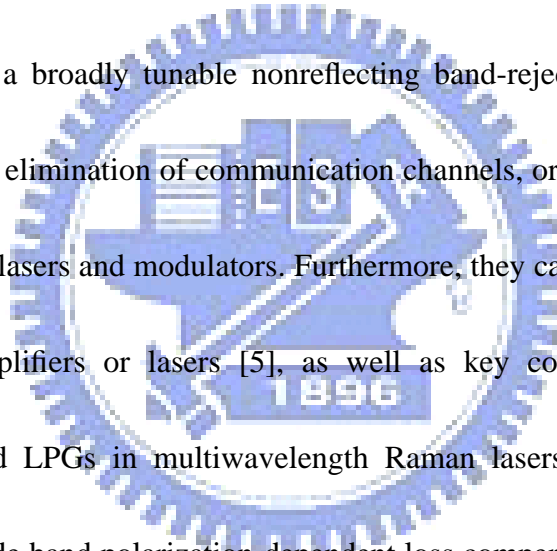
Fig. 1.4 A schematic diagram of a chirped fiber Bragg grating

#### 1.2.4.2 Long period grating

Long period fiber grating is a fiber device with typical grating periods ranging from several tens to several hundreds of micrometers. It is a kind of transmission grating based on the coupling between the fundamental core mode and the co-propagation cladding modes, and thus generates rejection bands in transmission spectrum. The coupling is highly efficient at a wavelength given by the phase matching condition  $\lambda = (n_{co} - n_{cl})\Lambda$  [32] where  $n_{co}$  and  $n_{cl}$  are the effective index of the core mode and cladding mode, respectively, and  $\Lambda$  is the grating period. To accomplish this, several fabrication techniques have been proposed. The first method used in germanium-doped fibers was the UV radiation [8-9]. However, since LPG require a large perturbation period in the range of 100  $\mu\text{m}$  - 1000  $\mu\text{m}$  and the spreading out of germanium-free photonic crystal fibers, other methods such as thermal and mechanical

pressure have been extensively explored in recent years [10].

Mechanically induced LPGs are of particular interest since they are versatile and can be implemented in almost any type of fiber. In mechanically induced LPG the fiber is subject to periodical stress, which results in alternated region under compression and stretching that modulate the refractive index via the photo-elastic effect. The main advantages of mechanically induced LPGs are the wide tuning range and bandwidth control, and they are erasable and reconfigurable [35]. These characteristics make mechanically induced LPGs an attractive option when a broadly tunable nonreflecting band-rejection filter is required for applications such as the elimination of communication channels, or to remove Stoke orders in cascaded Raman-based lasers and modulators. Furthermore, they can be used as dynamic gain equalizers in fiber amplifiers or lasers [5], as well as key components in tunable and reconfigurable cascaded LPGs in multiwavelength Raman lasers, all-fiber Mach–Zehnder interferometers, and wide band polarization-dependent loss compensators [36-37]. In addition, mechanically induced tunable LPGs could find applications in the fiber sensor field. Recently, P. Steinvurzel et al. reported a novel wide thermal tuning method in a mechanically induced long-period fluid-filled photonic-bandgap fiber grating [38], and this method promises potential applications in all-fiber temperature sensors. For all these applications it would be useful to develop simple and inexpensive flexible mechanically induced tunable LPGs.



### 1.3 Why long period grating made of photonic crystal

A key parameter in the LPG design is the type of optical fiber used. In this matter, photonic crystal fibers can offer unique properties such as endlessly single mode behavior, engineering dispersion, and highly polarization-dependent broadband coupling compared with standard step-index fibers [16]. Moreover, photonic crystal fibers have been demonstrated to be an adequate medium to implement LPGs. Compared with LPGs written in standard step-index fibers, photonic crystal fibers offer more stable performance against changes in temperature, strain, and the refractive index of the medium that surrounds the cladding [38]. All these features make photonic crystal fibers an excellent platform for the engineering of mechanically induced tunable LPGs.

In recent years, the development of photonic crystal fibers (PCFs) and their large number of potential applications have attracted a lot of interests. PCFs have several unique properties, but in this thesis we will focus on the supercontinuum generation and long period grating (LPG) by using photonic crystal fiber. We want to generate the ultra-wideband white light source by using photonic crystal fiber, and the broadband coherent light can be used in optical communication or medical applications.

LPGs can also be manufactured on PCFs. Methods used in the fabrication of long period gratings include UV radiation [8-9] and electric arc [10] technology. However, once LPG was fabricated onto the PCF, it is difficult to change the grating parameters such as central wavelength, rejection bandwidth, and transmission loss. For practical applications, it

would be useful to develop simple and inexpensive LPG with versatile tunability. The grating parameters will be varied by bending and tilting PCF under mechanical pressure.

#### **1.4 Why Q-switched mode-locked solid state laser**

High-peak power and short-pulse lasers are continuously interested in laser physicist because they have various practical applications. Generally, continuous wave mode-locking (CWML) is widely used technique in generating ultra short optical pulses. However, its repetition rate is restricted by the cavity length and is in tens of MHz. Due to these characteristics, the CW-ML pulses have various advantages such as such as wavelength conversion, supercontinuum generation [39], optical communication, optical switching, optical clocking, and nonlinear optical measurement. Nevertheless, high repetition rate pulses will accumulate heat in materials, leading to thermal lensing in optical nonlinearity measurements such as Z scan measurement. On the contrary, the Q-switched can generate lower repetition rates and higher pulse energies output. However, the generated Q-switched pulsewidth is comparative longer relative to the CW-ML pulses so that they have lower peak powers.

Simultaneously Q-switched and mode-locked (QML) lasers possess the superior property of high peak power over the CW mode-locked lasers but retain almost the same pulsewidth. The power of central ML peak pulse in the Q-switched envelope can be greatly

enhanced and the repetition rate of pulses is greatly reduced. Especially for picosecond (ps) mode-locked laser, which may not have enough peak intensity for achieving efficient wavelength conversion and supercontinuum generation, the QML provides a solution for these problems. Some methods like cavity dumping and regenerative amplifier have similar effect but their configurations are more complicated than the QML system.

## 1.5 Organization of the thesis

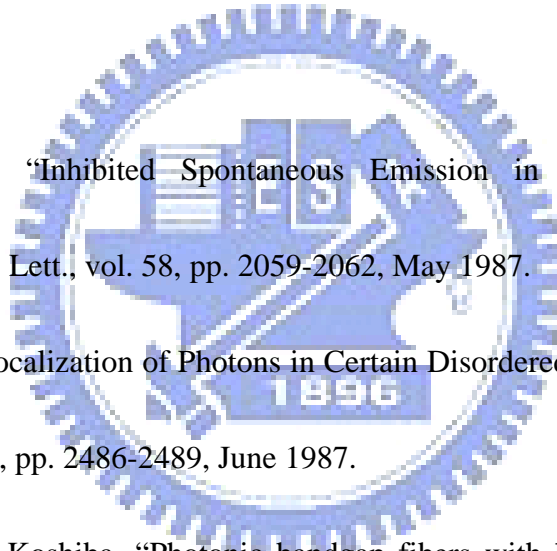
In Chapter 2, we will introduce the coupled-mode theory for LPGs and the theory of Q-switched mode-locking, as well as the methods of simulation for LPGs and Q-switched mode-locked lasers. Then in Chapter 3, we will introduce our experiment, including the experimental setup of LPGs and supercontinuum generation. The experimental setup of LPGs includes corrugated device, photonic crystal fiber, and unpolarized white light source. Experimental setup of SC generation includes pump laser system and setup of optics. Chapter 4 is the experimental results and discussions of LPGs. We will describe the stress-induced versatile tunable long-period grating in photonic crystal fibers. Chapter 5 is the experiment results and discussions of supercontinuum generation. We will describe Q-switched mode-locking of Nd:GdVO<sub>4</sub> laser with different initial transmittance, and the laser pulses are coupled into photonic crystal fiber to generate supercontinuum white-light source. Finally, we will give a brief conclusion and future works in Chapter 6.

## References

- [1] J.C. Knight, T.A. Birks, P.S. Russell, D.M. Atkin , “All-silica single-mode optical fiber with photonic crystal cladding, ” *Opt. Lett.* **21** (19) (1996) 1547–1549.
- [2] R. Holzwarth, T. Udem, T.W. Hansch, J.C. Knight, W.J. Wadsworth, P.S.J. Russell, “Optical frequency synthesizer for precision spectroscopy, ” *Phys. Rev. Lett.* **85** (2000) 2264–2267.
- [3] I. Hartl, X.D. Li, C. Chudoba, R.K. Ghanta, T.H. Ko, J.G. Fujimoto, J.K. Ranka, R.S.Windeler, “Ultrahighresolution optical coherence tomography using continuum generation in an air–silica microstructure optical fiber, ” *Opt. Lett.* **26** (2001) 608–610.
- [4] S. A. Diddams, D. J. Jones, J. Ye, S. T. Cundiff, J. L. Hall, J. K. Ranka, R. S. Windeler, R. Holzwarth, T. Udem, and T. W. Hänsch, “Direct link between microwave and optical frequencies with a 300 THz femtosecond laser comb, ” *Phys. Rev. Lett.* **84**, 5102-5105 (2000).
- [5] T. M. Monro, W. Belardi, K. Furusawa, J. C. Baggett, N. G. R. Broderick, and D. J. Richardson, “Sensing with microstructured optical fibres”, *Meas. Sci. Technol.* **12**, 854-858 (2001).
- [6] J. M. Fini, “Microstructure fibres for optical sensing in gases and liquids”, *Meas. Sci. & Tech.* **15**, 1120-1128 (2004).
- [7] T. Birks, D. Mogilevtsev, J. Knight, and P. Russell, “Dispersion compensation using single-material fibers,” *IEEE Photonics Technol. Lett.*, vol.11, no.6, pp.674–676, 1999.



- [8] P. F. Wysocki, J. B. Judkins, R. P. Espindola, M. Andrejco, and A. M. Vengsarkar, "Broad-band erbium-doped fiber amplifier flattened beyond 40 nm using long-period grating filter," *IEEE Photon. Technol. Lett.*, vo. 19, pp. 1343–1345, Oct. 1997.
- [9] V. Bhatia, D. Campbell, R. O. Claus, and A. M. Vengsarkar, "Simultaneous strain and temperature measurement with long-period gratings," *Opt. Lett.*, vol. 22, pp. 648–650, 1997.
- [10] A. M. Vengsarkar, P. J. Lemaire, J. B. Judkins, V. Bhatia, T. Erdogan, and J. E. Sipe, "Long-period fiber gratings as band-rejection filters," *J. Lightwave Technol.* **14**, 1996, pp. 58-65.
- [11] E. Yablonovitch, "Inhibited Spontaneous Emission in Solid-State Physics and Electronics," *Phys. Rev. Lett.*, vol. 58, pp. 2059-2062, May 1987.
- [12] S. John, "Strong Localization of Photons in Certain Disordered Dielectric Superlattices," *Phys. Rev. Lett.*, vol. 58, pp. 2486-2489, June 1987.
- [13] K. Saitoh and M. Koshiba, "Photonic bandgap fibers with high birefringence," *IEEE Photon. Technol. Lett.*, vol. 14, pp. 1291-1293, September 2002.
- [14] D. Ouzounov, D. Homoelle, and W Zipfel, "Dispersion measurements of microstructured fibers using femtosecond laser pulses," *Opt. Commun.*, vol. 192, pp. 219-223, June 1997.
- [15] T. M. Monro, D. J. Richardson, N. G. R. Broderick, and P. J. Bennett, "Holey Optical Fibers: An Efficient Modal Model," *J. Lightwave Technol.*, vol. 17, pp. 1093-1102, June 1999.



[16] T. A. Birks, J. C. Knight, and P. St. J. Russell, "Endlessly single-mode photonic crystal fiber," *Opt. Lett.* **22**, 961-963 (1997).

[17] J. C. Knight, J. Arriaga, T. A. Birks, A. Ortigosa-Blanch, W. J. Wadsworth, and P. St. J. Russell, "Anomalous dispersion in photonic crystal fiber", *Photonics Technol. Lett.* **12**, 807-809 (2000).

[18] R. F. Cregan, B. J. Mangan, J. C. Knight, T. A. Birks, P. S. J. Russell, P. J. Roberts, and D. C. Allan, "Single-mode photonic band gap guidance of light in air", *Science* **285**, 1537-1539 (1999)

[19] B. H. Lee, J. B. Eom, J. Kim, D. S. Moon, U.-C. Peak, and G.-H. Yang, "Photonic crystal fiber coupler," *Opt. Lett.*, vol. 27, pp. 812-814, May 2002.

[20] M. Stevenson, C. Martelli, J. Canning, B. Ashton and K. Lyytikainen, "Photonic crystal fibre optical attenuators," *Electron. Lett.*, vol. 41, pp. 1167-1169, October 2005.

[21] L. Zhang and C. Yang, "Polarization splitter base on photonic crystal fibers," *Opt. Express*, vol. 11, pp. 1015-1020, May 2003.

[22] A. Witkowska and M. Marciniak, "Nonlinear PCF as Dispersion Compensator in High-Bitrate Fiber Links," *The 6 International Conference on Transparent Optical Networks (ICTON 2004)*, vol. 2, pp. 234-237, July 2004

[23] J. M. Fini, "Microstructure fibres for optical sensing in gases and liquids," *Meas. Sci. & Tech.* **15**, 1120-1128 (2004).

[24] K. Morishita and Y. Miyake, "Fabrication and resonance wavelengths of long-period gratings written in a pure-silica photonic crystal fiber by the glass structure change," *J. Lightwave Technol.* **22**, 625-630 (2004)

[25] S. Coen, A. Hing Lun Chau, R. Leonhardt, J. D. Harvey, J. C. Knight, W. J. Wadsworth, and P. St. J. Russell, "White-light supercontinuum generation with 60-ps pump pulses in a photonic crystal fiber", *Opt. Lett.* **26**, 1356-1358 (2001).

[26] R. R. Alfano and S. L. Shapiro, "Emission in the region 4000 to 7000 Å Via Four-Photon Coupling in Glass," *Phys. Rev. Lett.*, **24**, 584 (1970).

[27] P. P. Ho, Q. X. Li, T. Jimbo, Y. L. Ku, and R. R. Alfano, "Supercontinuum pulse generation and propagation in a liquid carbontetrachloride," *Appl. Opt.*, **26**, 2700 (1987).

[28] J. K. Ranka, R. S. Windeler, and A. J. Stentz, "Visible continuum generation in air-silica microstructure optical fibers with anomalous dispersion at 800-nm," *Opt. Lett.*, **25**, 25 (2000)

[29] W. H. Reeves, D. V. Skryabin, F. Biancalana, J. C. Knight, P. S. Russell, F. G. Omenetto, A. Efimov, and A. J. Taylor, "Transformation and control of ultra-short pulses in dispersion-engineered photonic crystal fibers," *Nature*, **424**, 511 (2003).

[30] Turan Erdogan, "Fiber grating spectrum," *JOURNAL OF LIGHTWAVE TECHNOLOGY*, VOL. 15, NO. 8, AUGUST 1997

[31] P. F. Wysocki, J. B. Judkins, R. P. Espindola, M. Andrejco, and A. M. Vengsarkar, "Broad-band erbium-doped fiber amplifier flattened beyond 40 nm using long-period grating

filter,” IEEE Photon. Technol. Lett., vol 9, pp. 1343–1345, Oct. 1997.

[32] A. M. Vengsarkar, P. J. Lemaire, J. B. Judkins, V. Bhatia, T. Erdogan, and J. E. Sipe, “Long-period fiber gratings as band-rejection filters,” J. Lightwave Technol. **14**, 1996, pp. 58-65.

[33] V. Bhatia, D. Campbell, R. O. Claus, and A. M. Vengsarkar, “Simultaneous strain and temperature measurement with long-period gratings,” Opt. Lett., vol. 22, pp. 648–650, 1997.

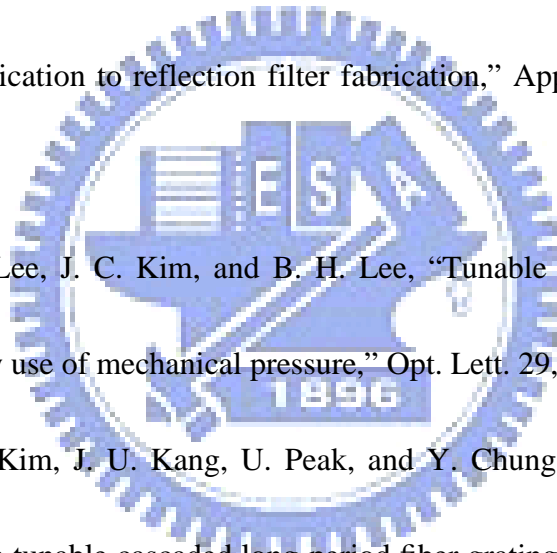
[34] K. O. Hill, Y. Fujji, D. C. Johnson, and B. S. Kawasaki, “Photo-sensitivity in optical fiber waveguides: Application to reflection filter fabrication,” Appl. Phys. Lett., vol. 32 pp. 647-649, 1978

[35] J. H. Lim, K. S. Lee, J. C. Kim, and B. H. Lee, “Tunable fiber grating fabricated in photonic crystal fiber by use of mechanical pressure,” Opt. Lett. **29**, 331–333 (2004)

[36] Y.-G. Han, C.-S. Kim, J. U. Kang, U. Peak, and Y. Chung, “Multiwavelength Raman fiber-ring laser based on tunable cascaded long-period fiber gratings,” IEEE Photon. Technol. Lett. **15**, 383–385 (2003).

[37] J. H. Iim, H. S. Jang, K. S. Lee, J. C. Kim, and B. H. Lee, “Mach–Zehnder interferometer formed in a photonic crystal fiber based on a pair of long-period fiber gratings,” Opt. Lett. **29**, 346–348 (2004).

[38] P. Steinvurzel, E. D. Moore, E. C. Mägi, and B. J. Eggleton, “Tuning properties of long period gratings in photonic bandgap fibers,” Opt. Lett. **31**, 2103–2105 (2006).



[39] J.-H. Lin, K.-H. Lin, C.-C. Hsu, W.-H. Yang, and Wen Feng Hsieh, "Supercontinuum generation in a microstructured optical fiber by picosecond self Q-switched mode-locked Nd:GdVO<sub>4</sub> laser," *Laser Phys. Lett.* **4**, 413-417 (2007).



## Chapter 2 Theory

### 2.1 Dispersion relation of PCF -- beam propagation method [1]

BPM is the most widely used propagation technique for modeling integrated and fiber optic photonic devices, and most commercial software for such modeling is based on it. There are several reasons for the popularity of BPM; perhaps the most significant being that it is conceptually straightforward, allowing rapid implementation of the basic technique, and it is also easy to use for anybody, even if he is not a specialist in BPM. Finally, the BPM technique is very flexible and extensible, allowing inclusion of most effects of interest (e.g. polarization, nonlinearities) by extensions of the basic method that fit within the same overall framework.

In this following section the basic approach is illustrated by formulating the problem under the restrictions of a scalar field (i.e. neglecting polarization effects) and paraxiality (i.e. propagation restricted to a narrow range of angles).

The scalar field assumption allows the wave equation to be written in the form of the well-known Helmholtz equation for monochromatic waves:

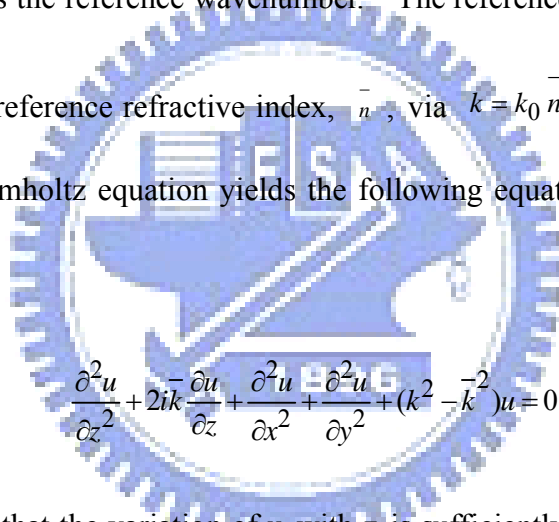
$$\frac{\partial^2 \phi}{\partial z^2} + \frac{\partial^2 \phi}{\partial x^2} + \frac{\partial^2 \phi}{\partial y^2} + k^2(x, y, z)\phi = 0 \quad (2.1-1)$$

where  $k(x, y, z) = k_0 n(x, y, z)$   $k_0 = \frac{2\pi}{\lambda}$  is wavenumber in free space,  $n(x, y, z)$  is the refractive index distribution in space.

Considering that in typical guided-wave problems the most rapid variation in the field is the phase variation due to propagation along the guiding axis, and assuming that axis is predominantly along the  $z$  direction, it is beneficial to factor this rapid variation out of the problem by introducing a so-called slowly varying field  $u(x, y, z)$  via the ansatz.

$$\phi(x, y, z) = u(x, y, z)e^{i\bar{k}z}, \quad (2.1-2)$$

where  $\bar{k}$  is a constant number to be chosen to represent the average phase variation of the field and is referred to as the reference wavenumber. The reference wavenumber is frequently expressed in terms of a reference refractive index,  $\bar{n}$ , via  $\bar{k} = k_0 \bar{n}$ . Introduction the above expression into the Helmholtz equation yields the following equation for the slowly varying field:



$$\frac{\partial^2 u}{\partial z^2} + 2i\bar{k} \frac{\partial u}{\partial z} + \frac{\partial^2 u}{\partial x^2} + \frac{\partial^2 u}{\partial y^2} + (k^2 - \bar{k}^2)u = 0 \quad (2.1-3)$$

It is now assumed that the variation of  $u$  with  $z$  is sufficiently slow so that the first term above can be neglected with respect to the second; this is the familiar slowly varying envelope approximation and in this context it is also referred to as the paraxial or parabolic approximation.

With this assumption and after slight rearrangement, the above equation reduces to:

$$\frac{\partial u}{\partial z} = \frac{i}{2k} \left\{ \frac{\partial^2 u}{\partial x^2} + \frac{\partial^2 u}{\partial y^2} + (k^2 - \bar{k}^2)u \right\} \quad (2.1-4)$$

This is the basic BPM equation in three dimensions (3D); simplification to two dimensions

(2D) is obtained by omitting any dependence on y. Given an input field,  $u(x,y,z=0)$ , the above equation determines the evolution of the field in the space  $z>0$ . The factoring of the rapid phase variation allows the slowly varying field to be represented numerically on a longitudinal grid (i.e. along z) that can be much coarser than the wavelength for many problems, contributing in part to the efficiency of the technique.

In the finite-difference approach, the approach is illustrated for a scalar field in 2D (xz); extension to 3D is then briefly summarized.

$$\frac{u_i^{n+1} - u_i^n}{\Delta z} = \frac{i}{2k} \left\{ \frac{\delta^2}{\Delta x^2} + \left( k(x_i, z_{n+\frac{1}{2}})^2 - k^2 \right) \right\} \frac{u_i^{n+1} + u_i^n}{2}, \quad (2.1-5)$$

where  $\delta^2$  represents the standard second order difference operator,

$$\delta^2 u_i = u_{i+1} + u_{i-1} - 2u_i, \text{ and } z_{n+\frac{1}{2}} = z_n + \frac{\Delta z}{2}.$$

The above equation can be rearranged into the form of a standard tridiagonal matrix equation for the unknown field  $u_i^{n+1}$  in terms of known quantities, resulting in:

$$a_i u_{i-1}^{n+1} + b_i u_{i+1}^{n+1} = d_i, \quad (2.1-6)$$

Expressions for the coefficients in the above are readily derived and can be found in (2.1-5).

The tridiagonal nature of Eq. (2.1-6) allows rapid solution in order  $O(N)$  operations, where N is the number of grid points in x.

The above numerical solution can be readily extended to 3D, however the direct extension of the Crank-Nicholson approach leads to a system of equations that is not tridiagonal, and



requires  $O(N_x^2 \cdot N_y^2)$  operations to solve directly which is non-optimal. Fortunately there is a standard numerical approach referred to as the alternating direction implicit which allows the 3D problem to be solved with optimal  $O(N_x \cdot N_y)$  efficiency.

In this and the previous section the concept and implementation details of the basic BPM method have been reviewed. In the following sections various methods for extending BPM are summarized, and details of numerical implementation can be found in the corresponding references

## 2.2 Coupled mode theory of long period grating [2]

The coupled mode theory is often used in waveguide optics. In the section, we will describe a coupled-wave analysis in which the periodic variation of dielectric tensor is considered as a perturbation that couples the unperturbed normal modes of propagation of the structure. The dielectric tensor as a function of space is written as

$$\varepsilon(x, y, z) = \varepsilon_a(x, y) + \Delta\varepsilon(x, y, z), \quad (2.2-1)$$

where  $\varepsilon_a(x, y)$  is the unperturbed part of the dielectric tensor, and  $\Delta\varepsilon(x, y, z)$ , representing the dielectric perturbation, is periodic in  $z$  direction and is the only small periodically varying part of the dielectric tensor.

If an arbitrary field of frequency  $\omega$  is excited at  $z = 0$ , the propagation of the field in

perturbed medium can always be expressed in terms of a linear combination of the normal modes:

$$E = \sum_m A_m(z) E_m(x, y) e^{j(\omega t - \beta_m z)} \quad (2.2-2)$$

where the expansion coefficients evidently depend on  $z$ , since for  $\Delta\epsilon(x, y, z) \neq 0$  the waves  $E = E_m(x, y) e^{j(\omega t - \beta_m z)}$  are no longer the eigenmodes. The  $z$  dependence of the amplitude  $A_m(z)$  is more reflection of the coupling of the normal modes.

Since the dielectric perturbation  $\Delta\epsilon(x, y, z)$  is periodic in  $z$ , we can expand it as a Fourier series

$$\Delta\epsilon(x, y, z) = \sum_{m \neq 0} \epsilon_m(x, y) e^{-jm \frac{2\pi}{\Lambda} z} \quad (2.2-3)$$

where the summation is over all integers  $m$ , except for  $m = 0$ , because of the definition of  $\Delta\epsilon(x, y, z)$  in equation (2.2-1).

We now substitute Equations (2.2-2) and (2.2-3) into the wave equation

$$\left\{ \nabla^2 + \omega^2 \mu [\epsilon_a(x, y) + \Delta\epsilon(x, y, z)] \right\} E = 0 \quad (2.2-4)$$

and, we further assume that the dielectric perturbation is weak, so that the variation of the mode amplitudes is slow and satisfies the condition, slowly varying amplitude (SVA) approximation.

$$\frac{\partial^2 A_m}{\partial z^2} \ll \beta_m \frac{\partial A_m}{\partial z} \quad (2.2-5)$$

Therefore, we can obtain

$$\frac{dA_k}{dz} = -j \frac{|\beta_k|}{\beta_k} \sum_m \sum_n C_{kn}^{(m)} A_n(z) e^{j(\beta_k - \beta_n - m \frac{2\pi}{\Lambda})z} \quad (2.2-6)$$

where the coupling coefficients  $C_{kn}^{(m)}$  are defined as

$$C_{kn}^{(m)} = \frac{\omega}{4} \langle k | \epsilon_m(x, y) | n \rangle = \frac{\omega}{4} \int_{-\infty}^{\infty} E_k^*(x, y) \epsilon_m(x, y) E_n(x, y) dx dy \quad (2.2-7)$$

The coefficient  $C_{kn}^{(m)}$  reflects the magnitude of the coupling between the k-th and n-th modes due to the m-th Fourier component of the dielectric perturbation.

Equation (2.2-6) describes the most general case of mode coupling due to a periodic dielectric perturbation. In practice, often only the coupling between two modes is involved. We consider coupling between  $E_1(x, y)e^{j(\omega t - \beta_1 z)}$  and  $E_2(x, y)e^{j(\omega t - \beta_2 z)}$  neglecting interaction with any other modes, the coupled equations become

$$\begin{aligned} \frac{dA_1}{dz} &= -j \frac{\beta_1}{|\beta_1|} C_{12}^{(m)} A_2(z) e^{j\Delta\beta z}, \\ \frac{dA_2}{dz} &= -j \frac{\beta_2}{|\beta_2|} C_{21}^{(-m)} A_1(z) e^{-j\Delta\beta z}, \end{aligned} \quad (2.2-8)$$

where

$$\Delta\beta = \beta_1 - \beta_2 - \frac{2\pi}{\Lambda} \quad ,$$

(2.2-9)  $C_{12}^{(m)}$  and  $C_{21}^{(-m)}$  are the coupling coefficients given by equation (2.2-7), and  $\Lambda$  is the period of grating. It can be easily proved that  $C_{12}^{(m)} = [C_{21}^{(-m)}]^*$ .

When the coupled modes are propagating in the same direction, the +z direction, the sign factors  $\frac{\beta_1}{|\beta_1|}$  and  $\frac{\beta_2}{|\beta_2|}$  are both equal to 1. The coupled equations (2.2-8) become

$$\begin{aligned}\frac{dA_1}{dz} &= -j\kappa A_2(z)e^{j\Delta\beta z} \\ \frac{dA_2}{dz} &= -j\kappa^* A_1(z)e^{-j\Delta\beta z}\end{aligned}\quad (2.2-10)$$

where the coupling constant is written as  $\kappa = C_{12}^{(m)}$ ,

By taking derivative of Equation (2.2-10) with respect to  $z$  to remove the coupled terms, Equation (2.2-10) becomes second-order ordinary differential equations. The general solutions for  $A_1$  and  $A_2$  can easily be obtained. After a few steps of algebra, the general solutions can be written

$$\begin{aligned}A_1(z) &= e^{j\frac{\Delta\beta}{2}z} \cdot \left[ \left( \cos sz - j\frac{\Delta\beta}{2} \cdot \frac{\sin sz}{s} \right) A_1(0) - j\kappa \frac{\sin sz}{s} A_2(0) \right] \\ A_2(z) &= e^{-j\frac{\Delta\beta}{2}z} \cdot \left[ -j\kappa^* \frac{\sin sz}{s} A_1(0) + \left( \cos sz + j\frac{\Delta\beta}{2} \cdot \frac{\sin sz}{s} \right) A_2(0) \right]\end{aligned}\quad (2.2-11)$$

where

$$s^2 = \kappa \cdot \kappa^* + \left( \frac{\Delta\beta}{2} \right)^2 \quad (2.2-12)$$

and  $A_1(0)$  and  $A_2(0)$  are the mode amplitudes at  $z = 0$ .

We assume that single-beam incidence at  $z = 0$ , so  $A_2(0) = 0$ , the solutions become

$$\begin{aligned}A_1(z) &= e^{j\frac{\Delta\beta}{2}z} \cdot \left( \cos sz - j\frac{\Delta\beta}{2} \cdot \frac{\sin sz}{s} \right) A_1(0) \\ A_2(z) &= e^{-j\frac{\Delta\beta}{2}z} \cdot \left( -j\kappa^* \frac{\sin sz}{s} \right) A_1(0)\end{aligned}\quad (2.2-13)$$

where  $s^2 = \kappa \cdot \kappa^* + \left( \frac{\Delta\beta}{2} \right)^2$

We can define the coupling efficiency as

$$\eta = \frac{|A_2(L)|^2}{|A_1(0)|^2}, \quad (2.2-14)$$

where L is the interaction length. Using equations (2.2-12) and (2.2-13), we obtain

$$\eta = \frac{|\kappa|^2}{|\kappa|^2 + \left(\frac{\Delta\beta}{2}\right)^2} \cdot \sin^2\left(|\kappa|L \cdot \sqrt{1 + \left(\frac{\Delta\beta}{2|\kappa|}\right)^2}\right) \quad (2.2-15)$$

so we know the transmission spectrum obtained from (2.2-15)

$$T = 10 \times \text{Log}\left[1 - \frac{|\kappa|^2}{|\kappa|^2 + \left(\frac{\Delta\beta}{2}\right)^2} \cdot \sin^2\left(|\kappa|L \cdot \sqrt{1 + \left(\frac{\Delta\beta}{2|\kappa|}\right)^2}\right)\right] \quad (2.2-16)$$

Finally, we use the dispersion of PCF and set proper coupling coefficient, the transmission of LPGs can be obtained from this formula. Results of the constant period long period grating of transmission spectrum will be shown in chapter 5.

### 2.3 Model for passively Q-switched laser with simultaneous mode-locking

In the section, we will show the temporal change of photon density derived by many pioneers such as John J. Degnan [3], Michael Bass [4], YF Chen [5]. The case we discussed is the laser with an intra-cavity saturable absorber. The following coupled rate equations describe the laser operation including laser rod, saturable absorber and resonator mirrors:

$$\frac{d\Phi}{dt} = \frac{\Phi}{t_r} \{2\sigma n l - 2\sigma_{gs} n_{gs} l_s - 2\sigma_{es} n_{es} l_s - [\ln(\frac{1}{R}) + L]\} \quad (2.3-1)$$

$$\frac{dn}{dt} = -\gamma c \sigma \Phi n \quad (2.3-2)$$

$$\frac{dn_{gs}}{dt} = -\frac{A}{A_s} c \sigma_{gs} \Phi n_{gs} \quad (2.3-3)$$

For Q-switching mode-locking state, the temporal profile of photon density can be expressed as

$$\Phi(t) = \sum_{m=0} \Phi_m f(t-t_m) \quad (2.3-4)$$

where  $t_m = m t_r$ , with  $t_r$  being the round trip time,  $m$  the number of round trip,  $\Phi_m$  the relative amplitude of the mode locked pulses at  $m$ -th roundtrip, and  $f(t)$  assumed to be a sharp pulse centered at  $t=0$  which falls off rapidly in a time short compared to the resonator round trip transit time.

Consider the excited state absorption (ESA) effect in a four-level saturable absorber, the relative amplitude of the mode-locked pulses at time  $t_m = m t_r$  after an additional roundtrip through the cavity is given by

$$\Phi_m = \Phi_{m-1} \exp \{2\sigma n(t_m) l - 2\sigma_{gs} n_{gs}(t_m) l_s - 2\sigma_{es} n_{es}(t_m) l_s - [\ln(\frac{1}{R}) + L]\} \quad (2.3-5)$$

where  $\sigma$  is the simulated emission cross section of the gain medium,  $n(t_m)$  is the population density of the gain medium at the  $m$ -th roundtrip,  $l$  is the length of the gain medium,  $\sigma_{gs}$  is ground-state absorption (GSA) cross section in the saturable absorber,  $\sigma_{es}$  is ESA cross

section in the saturable absorber,  $n_{gs}(t_m)$  is the absorber ground-state population density at the m-th roundtrip,  $n_{es}(t_m)$  is absorber excited-state population density in the m-th roundtrip, R is reflectivity of the output mirror, and L is unsaturated intracavity roundtrip dissipative optical loss, respectively.

Introduction the variable  $\beta = \frac{\sigma_{es}}{\sigma_{gs}}$  and using the condition  $n_{gs}(t_m) + n_{es}(t_m) = n_{so}$ , Eq.

(2.3-5) can be rewritten as

$$\Phi_m = \Phi_{m-1} \exp\{2\sigma n(t_m)l - [2(1-\beta)\sigma_{gs}n_{gs}(t_m)l_s + \beta \ln(\frac{1}{T_0})] - [\ln(\frac{1}{R}) + L]\} \quad (2.3-6)$$

where  $n_{so}$  is the total density of the absorber and  $T_0 = \exp(-\sigma_{gs}n_{so}l_s)$  is the initial transmission of the saturable absorber. Note that the condition is an assumption introduced by Hercher [6] and adopted by Xia and Bass [4] to simplify the analysis of passive saturable absorbers. This condition assumes:

1. the upper terminal level of the GSA relaxes infinitely fast (relative to the temporal duration of the optical pulse) to the lower level of the ESA.
2. the upper terminal level of the ESA behaves similarly. Namely, it is assumed that the saturable absorber atomic populations are totally contained in either the ground or excited states during the interaction with the optical pulse.

These approximations may not be valid for very short mode-locked pulse-widths.

Since the Q-switched laser output pulses are much shorter than both the spontaneous lifetime and the pump period (time between output pulses), spontaneous relaxation and pumping can be safely neglected during the development of the output pulse. Therefore, the equation for the time rate of change of the population inversion density can be expressed as Eq. (2.3-2) where  $c$  is the speed of light and  $\gamma$  is the inversion reduction factor.

Dividing Eq. (2.3-2) by  $n$ , using (2.3-4) and normalized function

$$\int_{-\infty}^{\infty} c \sigma f(t) dt = 1 \quad (2.3-7)$$

and integration over time from zero to  $t_m$ ,  $n(t_m)$  is given by

$$n(t_m) = n(0) \prod_{k=0}^{m-1} \exp(-\gamma \Phi_k) \quad (2.3-8)$$

where  $n(0)$  is the initial population inversion density in the gain medium. It can be determined from the condition that the round-trip gain is exactly equal to the round-trip losses just before the Q-switch opens, thus

$$n(0) = \frac{\ln\left(\frac{1}{T_0^2}\right) + \ln\left(\frac{1}{R}\right) + L}{2\sigma l} \quad (2.3-9)$$

The equation for the time rate of change of the absorber ground state population density is given by Eq. (2.3-3), where  $A/A_s$  is the ratio of the effective area in the gain medium and in the saturable absorber. Divide Eq. (2.3-2) by (2.3-3) and integrate to give



$$n_{gs} = n_{so} \left[ \frac{n(t_m)}{n(0)} \right]^\alpha \quad (2.3-10)$$

$$\text{where } \alpha = \frac{1}{\gamma} \frac{\sigma_{gs}}{\sigma} \frac{A}{A_s} \quad (2.3-11)$$

The parameter  $\alpha$  indicates how fast the saturable absorber is bleached. The larger the  $\alpha$  parameter, the faster the saturable absorber is bleached. Substituting Eqs. (2.3-8)-(2.3-10) into Eq. (2.3-6), the recurrence relation for  $\Phi_m$  is given by:

$$\begin{aligned} \Phi_m = & \Phi_{m-1} \exp \left\{ \left[ \prod_{k=0}^{m-1} \exp(-\gamma\Phi_k) - 1 \right] \left[ \ln\left(\frac{1}{R}\right) + L \right] \right. \\ & \left. + \left[ \prod_{k=0}^{m-1} \exp(-\gamma\Phi_k) - [\beta - (1-\beta) \prod_{k=0}^{m-1} \exp(-\gamma\Phi_k)] \right] \ln\left(\frac{1}{T_0}\right) \right\} \end{aligned} \quad (2.3-12)$$

in terms of  $\Phi(t)$ , and the instantaneous power coupled from the output mirror is given by

Degnan [3]:

$$P(t) = \frac{h\nu A l^3}{t_r} \ln\left(\frac{1}{R}\right) \Phi(t) \quad (2.3-13)$$

where  $h\nu$  is the laser photon energy and  $A l^3$  is the cavity volume occupied by photons.

Substituting Eq. (2.3-12) into Eq. (2.3-13), the output power can be expressed as

$$P(t) = \frac{h\nu A c}{2} \ln\left(\frac{1}{R}\right) \sum_{m=0}^{\infty} \varphi_m f(t - t_m) \quad (2.3-14)$$

In this simulation, we use hyperbolic secant as our pulse shape  $\phi(t) \sim \text{sech}^2(t/\tau_p)$ , where the parameter  $\tau_p$  is related to the FWHM mode-locked pulse-width by  $\tau$  (FWHM) = 1.76 $\tau_p$  [7].

Thus, we can simulate the temporal profile of Q-switching mode-locking pulse by (2.3-14) and

we will present the results later in Chapter 6.



## References

- [1] RSoft Design Group, Inc., “*BeamPROP 5.1.1*”
- [2] Amnon Yariv, Pochi Yeh, “*Photonic*” (Oxford New York, 2007)
- [3] John J. Degnan, “Optimization of passively Q-switched lasers,” *IEEE J. Quantum Electron.* **31**, 1890 (1995).
- [4] Guohua Xiao, Michael Bass, “A generalized model for passively Q-switched lasers including excited state absorption in the saturable absorber,” *IEEE J. Quantum Electron.* **33**, 41 (1997).
- [5] Yung-Fu Chen and S. W. Tsai, “Simultaneous Q-Switching and Mode-Locking in a Diode-Pumped Nd :YVO<sub>4</sub>-Cr<sup>4+</sup> :YAG Laser,” *IEEE J. Quantum Electron.* **37**, 580 (2001).
- [6] M. Hercher, “An analysis of saturable absorbers,” *Appl. Opt.*, **6**, 947 (1967).
- [7] A. E. Siegman, “*Lasers. Mill Valley*,” CA: Univ. Sci. Books, **1122** (1986).

## Chapter 3 Experimental

### 3.1 Experimental setup of LPG

#### 3.1.1 Corrugated devices

The novel corrugated devices for making LPGs are constructed by two methods. The first is to construct the device by wrapping a long copper wire on a cylindrical metallic post as shown in Fig. 3-1 (a). The diameter of copper wire is  $400\ \mu\text{m}$ , and consequently the periodicity of the corrugated device is also  $400\ \mu\text{m}$ . The second is to construct the device by engraving periodic parallel V-grooves on a metallic plate. The periodically grooved plate, as shown in Fig. 3-1 (b), has V-grooves of about  $200\ \mu\text{m}$  in depth and period of  $400\ \mu\text{m}$  on a  $6\ \text{cm} \times 1\ \text{cm}$  metal surface.

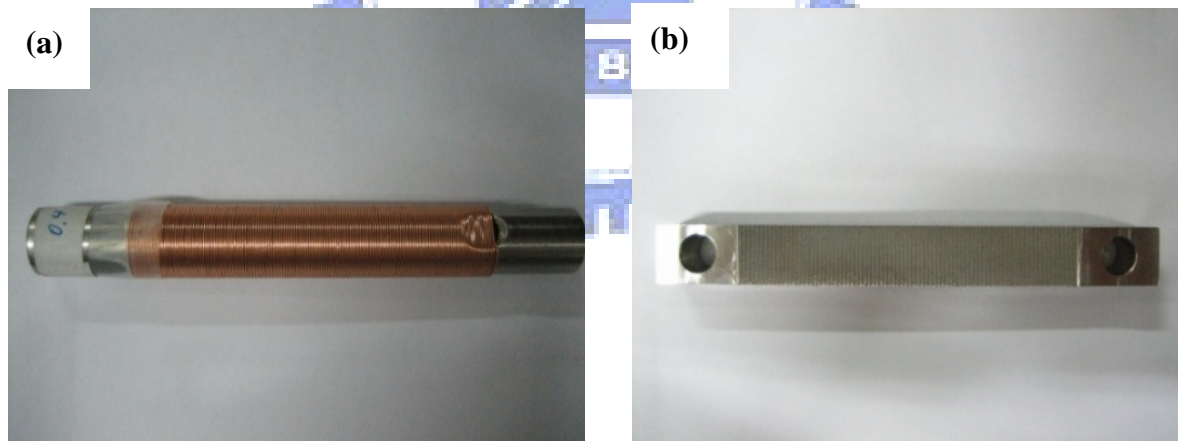


Fig. 3-1 novel corrugated devices: wrapping a long copper wire on a cylindrical metallic post (left), and V-grooved plate (right)

### 3.1.2 Photonic crystal fiber

In LPGs experiment, we used an endlessly-single-mode photonic crystal fiber ESM-12-01 from Blaze Photonics. The arrangement of the air holes are hexagonal, and the cross sectional scanning electron microscope image (SEM) of the fiber is shown in Fig. 3-2. The core diameter of the photonic crystal fiber is about  $12\ \mu\text{m}$ , surrounded by four rings of holes and the diameter of holes is about  $4\ \mu\text{m}$ . The pitch (spacing between adjacent holes) is about  $8\ \mu\text{m}$ , and its outside diameter and coating diameter are  $125\ \mu\text{m}$  and  $225\ \mu\text{m}$ , respectively. The attenuation spectrum of this fiber shows an attenuation peak near  $1400\ \text{nm}$ .

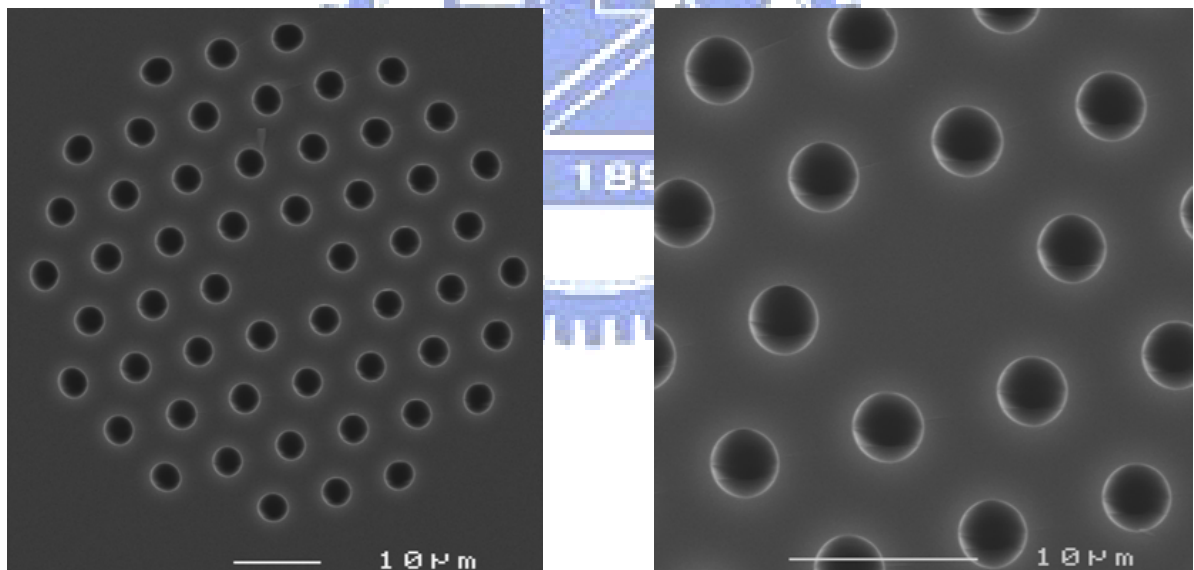


Fig. 3-2 Scanning electron microscope image of photonic crystal fiber cladding (left) and core region (right).

### 3.1.3 Un-polarized white light source

In order to measure the transmission spectrum as LPG induced in PCF, we use a light bulb as the light source. The light bulb is an un-polarized white-light source and is launched into the fiber link as shown in Fig. 3-3.

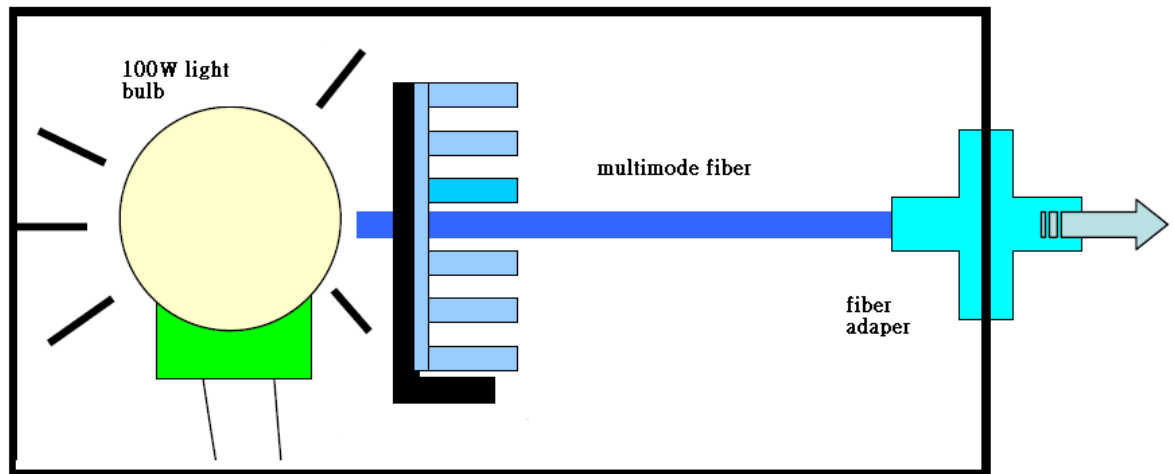


Fig. 3-3 Structure of un-polarized white-light source.

### 3.1.4 Measurement of transmission spectra of LPG

In our experiment, when mechanical stress is applied and increased gradually, we record the transmission spectra of the induced PCF-LPG by launching an unpolarized white-light source (WLS) into one end of the PCF, while the other end is connected to an optical spectral analyzer (OSA) (Ando AQ-6315).

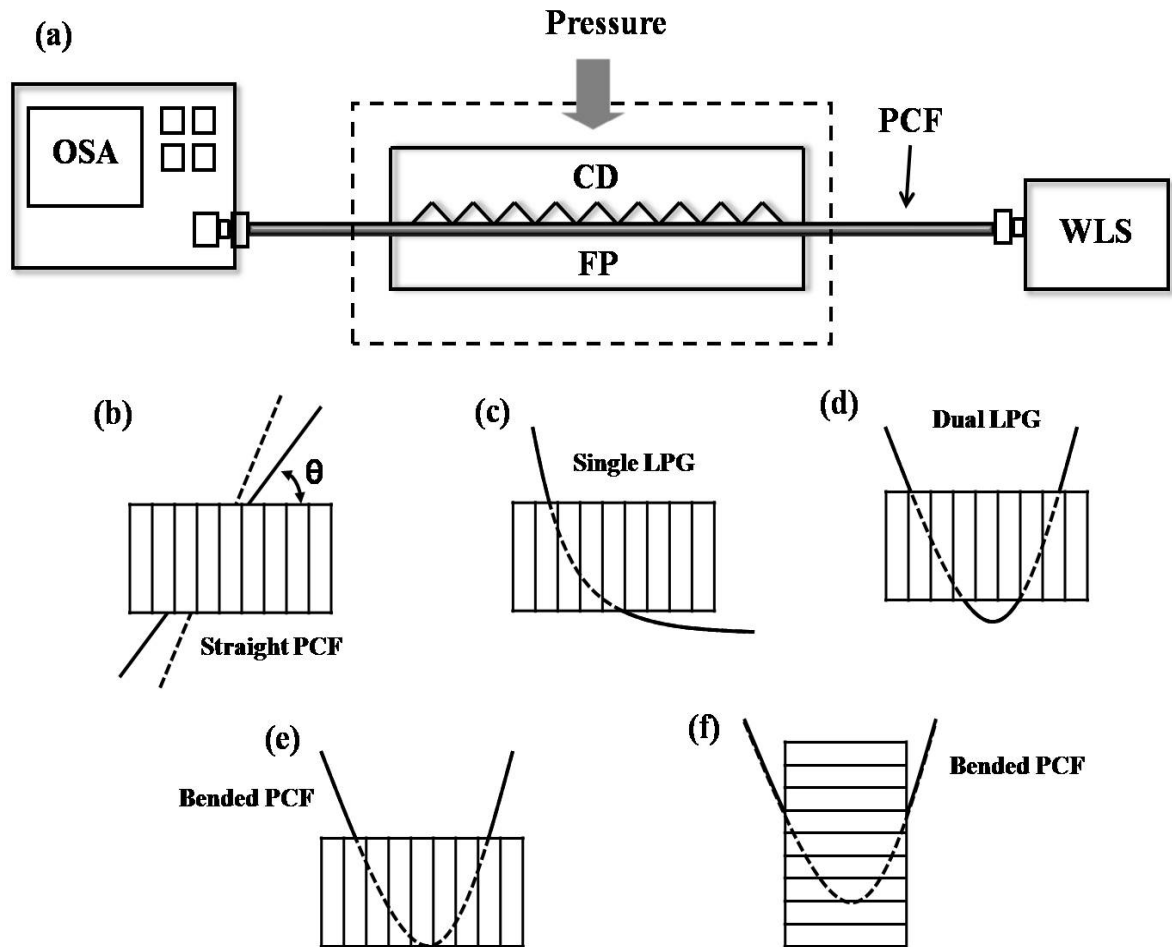
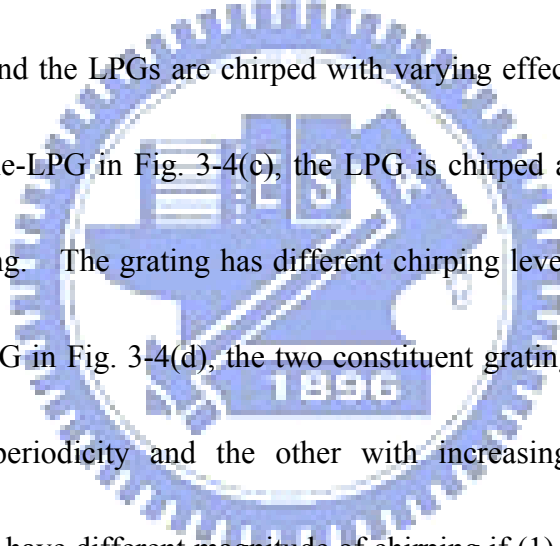


Fig. 3-4. (a) Schematic of the experimental setup and generation of LPGs in PCFs by mechanical stress onto corrugated device. WLS: unpolarized white light source, OSA: optical spectrum analyzer, CD: corrugated device, FP: flat plate. (b) Constant period LPG made by using corrugated device, (c) Single-LPGs can be induced by pressing one part of the banded PCF, (d) Dual-LPGs can be induced simultaneously by pressing two separate parts of the banded PCF, (e) Chirped single-LPG, (f) Chirped single-LPG by rotating 90 degrees of the V-grooved metallic plate.

As shown in Fig. 3-4, LPGs are induced in PCF when mechanical stress is applied. A constant-period LPG can be obtained if the PCF is straight [Fig. 3-4(b)]. However, LPGs become chirped (i.e., with continuously changed periodicity) when PCF is bended [Fig. 3-4(c)-(f)] with properly translating or rotating the corrugated device (V-grooved plate or wrapping a long copper wire on a cylindrical metallic post). Either single-LPG [Fig. 3-4(c)] or dual-LPG [Fig. 3-4(d)] can be generated in the bended PCF. The amount of chirping is controlled by the curvature of bended PCF as well as the angle of the corrugated device against the fiber axis, and the LPGs are chirped with varying effective grating periods along the PCF. For the single-LPG in Fig. 3-4(c), the LPG is chirped and the effective period is varying along the grating. The grating has different chirping level between the two ends of the LPG. For dual-LPG in Fig. 3-4(d), the two constituent gratings have opposite chirping, one with decreasing periodicity and the other with increasing periodicity. These two constituent gratings can have different magnitude of chirping if (1) an asymmetrically bended PCF is pressed by the corrugated device, or (2) a symmetrically bended PCF is pressed by a rotated corrugated device.



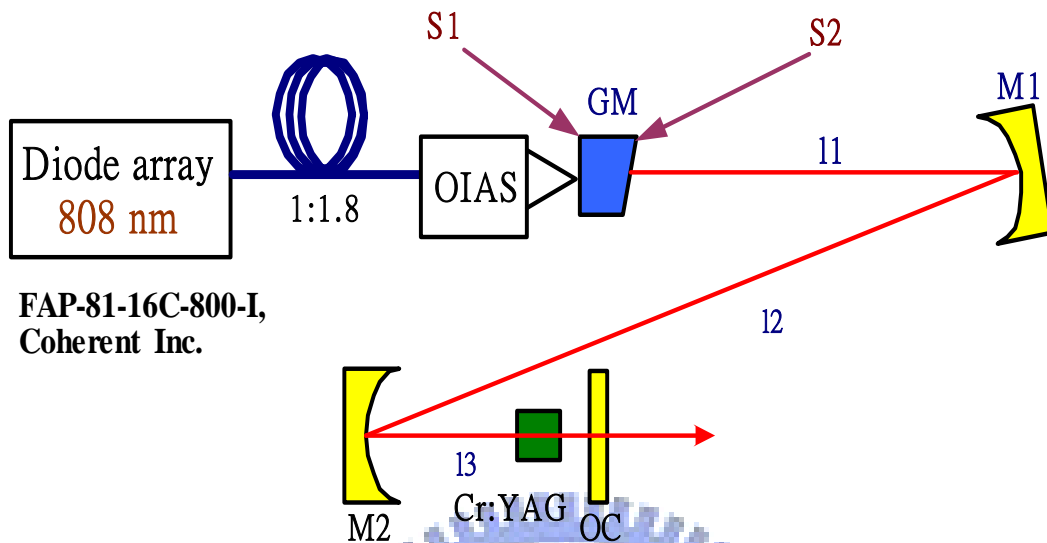
## **3.2 Experimental setup of Supercontinuum**

### **3.2.1 Q-switched mode-locked laser**

The schematic setup of our laser with z-configuration is shown in Fig. 3-5. A fiber-coupled diode array laser (FAP-81-16C-800-I, Coherence Inc.) with center wavelength



of 808 nm was used as the pump source.



**FAP-81-16C-800-I,  
Coherent Inc.**

Fig. 3-5 Schematic diagram of diode-pumped Q-switched mode-locked Nd:GdVO<sub>4</sub> laser. GM is gain medium (Nd:GdVO<sub>4</sub>), M<sub>1</sub> and M<sub>2</sub> are folding mirrors and OC is the output coupler.

The output beam from the fiber was imaged on the laser crystal, which is a 4x4x8 mm<sup>3</sup> a-cut Nd:GdVO<sub>4</sub> crystal (with 0.5% Nd<sup>3+</sup> concentration) through an 1:1.8 optical imaging accessory (OIA's, Coherent Inc.). In order to reduce the thermal loading in the laser crystal and hence prevent it from possible thermal fracture, the Nd:GdVO<sub>4</sub> crystal was wrapped with indium foil and held in a copper block which was cooled by using thermoelectric cooler. The surface temperature of the Nd:GdVO<sub>4</sub> crystal was controlled, being held at 15<sup>0</sup>C. One side of the laser crystal (S<sub>1</sub>) is high reflection (HR) coated at 1064 nm and anti-reflection (AR) coated at 808 nm as an end mirror of the resonator; while the other side (S<sub>2</sub>) with 2 degree wedge is AR coated at 1064 nm. Two curved mirrors M<sub>1</sub> and M<sub>2</sub>, with radii of curvatures of 500 mm and 200 mm, were used as folding mirror to conduct cavity beam through a

Cr<sup>4+</sup>:YAG to output coupler (OC). We choose different combinations of OC with reflectivity of 60% and 80% at 1064 nm, and Cr<sup>4+</sup>:YAG saturable absorber with initial transmittance T<sub>0</sub> of 80%, 55% and 40% to optimize the generated QML pulses.

The output of the Nd:GdVO<sub>4</sub> laser from either OC or the wedged facet of the laser crystal was measured by a power meter (Ophir Inc.) or detected by a high speed InGaAs detector (Electro-Physics Technology, ET 3000) that was connected to the oscilloscope (LeCroy LT372, bandwidth 500 MHz) or an optical spectrum analyzer (Ando AQ-6315) with resolution of 0.01 nm. A noncollinear autocorrelator containing a 2-mm thick type-I BBO was used to measure the pulsewidth as shown in Fig. 3-6.

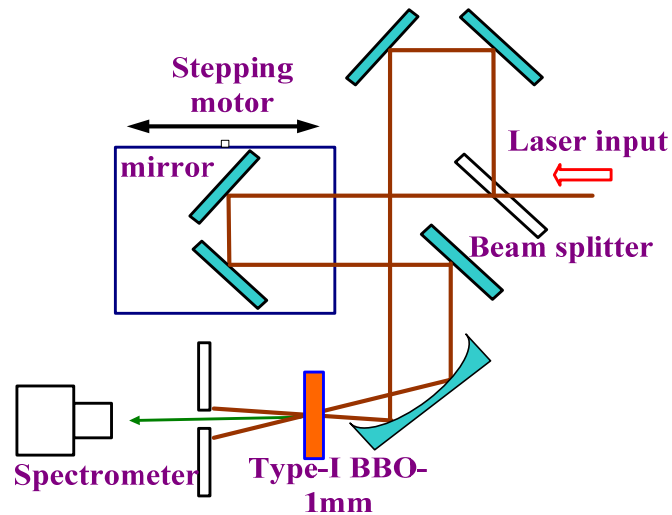


Fig. 3-6 Schematic diagram of noncollinear autocorrelator.

### 3.2.2 Supercontinuum generation

In our experiment, the pumping source, passively mode-locked Nd:GdVO<sub>4</sub> laser, is focused into a 1 m-long PCF with about 35% coupling efficiency by a 40X microscope objective lens. The core diameter of the used PCF is about 1.7  $\mu\text{m}$  and the pitch  $\Lambda$  (spacing between adjacent holes) is about 1.4  $\mu\text{m}$ . The diameter of holes is about 0.6  $\mu\text{m}$  except for the two holes near the core whose diameter is about 0.7  $\mu\text{m}$ . The fiber has quite high nonlinearity with nonlinear coefficient  $\gamma$  being  $74 \text{ km}^{-1} \cdot \text{W}^{-1}$  due to its small core diameter. It is also polarization maintaining because of its asymmetric arrangement of the holes near the core. It also has two zero dispersion points which are located at 760 nm and 1160 nm. The used pump wavelength is in the anomalous dispersion region. The experiment setup is shown in Fig. 3-7. A  $\lambda/2$  plate is used to change the polarization state of the laser to get the widest spectral broadening. Finally we measured the output spectrum using an optical spectrum analyzer (Ando AQ-6315).

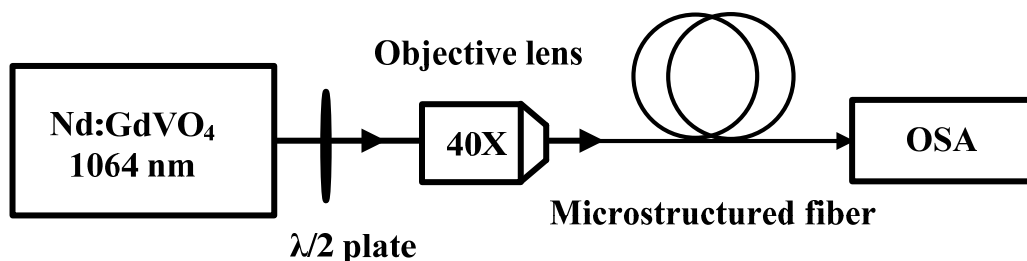


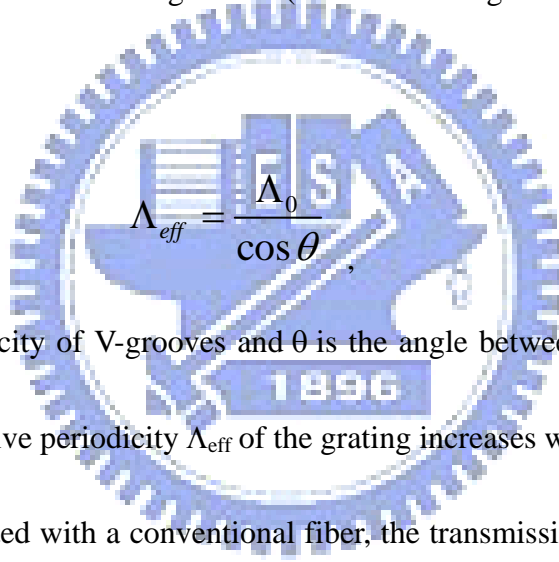
Fig. 3-7 The experimental setup of supercontinuum generation.

# Chapter 4 Stress-Induced Versatile Tunable Long-Period Grating in Photonic Crystal Fibers

## 4.1 Transmission spectra of LPGs made by V-grooved plate

### 4.1.1 Constant LPG

Constant period LPGs can be obtained if the PCF is straight, and we can vary the fiber grating period by tilting the angle of the V-grooved plate against the axes of straight PCFs as shown in Fig. 3-4 (b). In this configuration (as shown in Fig. 4-1), the effective periodicity is given as


$$\Lambda_{eff} = \frac{\Lambda_0}{\cos \theta}, \quad (4.1-1)$$

where  $\Lambda_0$  is the periodicity of V-grooves and  $\theta$  is the angle between PCF and the normal of V-grooves. The effective periodicity  $\Lambda_{eff}$  of the grating increases with the tilting angle  $\theta$ .

For a LPG fabricated with a conventional fiber, the transmission spectrum has dip at the wavelength corresponding to resonance with various cladding modes, and the resonance wavelength increases with increasing grating periodicity [1]. However, the resonance wavelength of PCF-LPG decreases with increasing grating periodicity, as shown in Fig. 4-2. The center wavelength of LPG can be tuned from 790 nm to 1590 nm as the effective period is reduced from 805  $\mu\text{m}$  to 470  $\mu\text{m}$ .

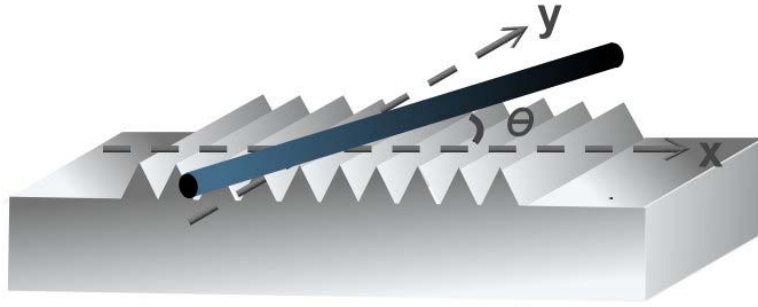


Fig. 4-1 Schematic of the mechanism for tuning the grating periodicity.

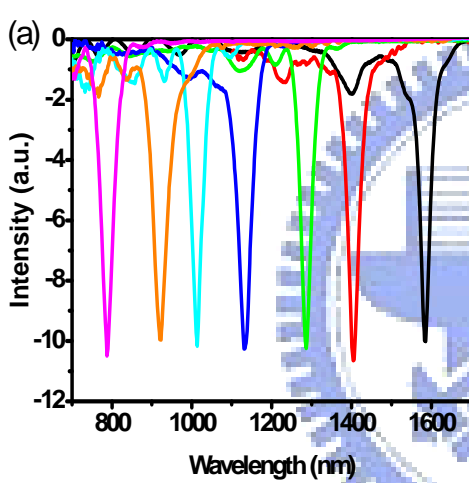


Fig. 4-2. Measured transmission spectra of constant-period gratings obtained by adjusting the angle between the straight PCF and the V-grooves.

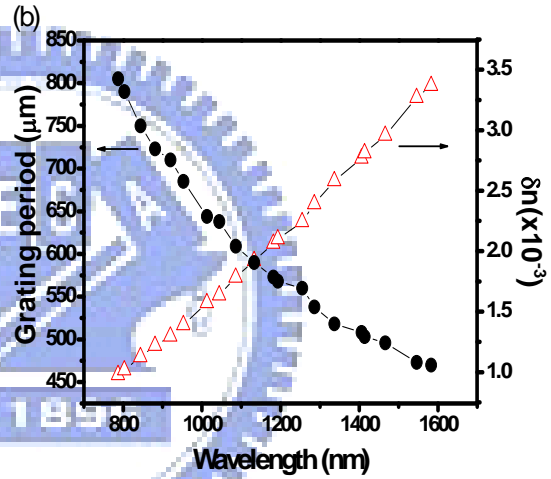


Fig. 4-3. Resonant wavelengths measured at different grating periods, as well as the calculated effective indices differences with respect to resonance wavelengths.

By measuring the resonant wavelengths of the LPGs, the differences in the effective indices of the core mode and the cladding modes are obtained. According to the coupled-mode theory, the resonance wavelength  $\lambda_{\text{res}}$  and the effective grating pitch  $\Lambda_{\text{eff}}$  are related by the phase-matching condition:

$$\lambda_{\text{res}} = \Lambda_{\text{eff}} [n_{\text{eff}}^{\text{co}}(\lambda) - n_{\text{eff}}^{\text{clad}}(\lambda)] , \quad (4.1-2)$$

where the effective indices of the core mode  $n_{\text{eff}}^{\text{co}}(\lambda)$  and the cladding modes  $n_{\text{eff}}^{\text{clad}}(\lambda)$  can be obtained as functions of the resonant wavelength. As shown in Fig. 4-3, the difference of effective index,  $\delta n$ , of the core mode and cladding modes is in the order of  $10^{-3}$ , and increases with the central rejection wavelength. Fig. 4-3 also shows that the central wavelength increases as the grating period decreases. Transmission loss of the constant-period LPG can be increased to 18 dB, however, the PCF will be broken if the applied mechanical stress is too large.

#### 4.1.2 Chirped LPGs

By properly translating the grooved plate, chirped LPGs can also be generated in a symmetrically bended PCF by pressing the PCF with a constant period V-grooved plate as in the configurations of Fig. 3-4(e) and Fig. 3-4(f). The amount of chirping is controlled by the curvature of PCF, as well as the angle of the grooved plate against the fiber sections.

Fig. 4-4(a) shows the transmission spectra of various chirped single-LPGs. The transmission spectra in Fig. 4-4(a) are obtained from the bended PCFs as in Fig. 3-4(e) for different curvatures with curve (1) < curve (2) < curve (3). Due to the bending of PCF, the periodicity of LPG along PCF decreases first, and then increases. As the curvature of PCF increases, the amount of chirping and effective periodicity will increase, leading to the

broadening of spectral dip in the transmission spectrum [Fig. 4-4(a)] and the resonant wavelength is shifted from 1447 nm to 1137 nm. The 3-dB rejection bandwidth is changed from 131 nm to 250 nm. Figure 4-4(b) shows the transmission spectra for the chirped single-LPG when the V-grooved metallic plate is rotated by 90 degrees as in Fig. 3-4(f). In this case, the periodicity of LPG along PCF increases first, and then decreases, which is contrary to Fig. 3-4 (e). The results in Fig. 4-4 (b) are obtained for bended PCF of different curvatures: curve (4) < curve (5) < curve (6). The center wavelength of this PCF-LPG is shifted from 1363 nm to 1549 nm, and the 3-dB rejection bandwidth is changed from 147 nm to 195 nm.



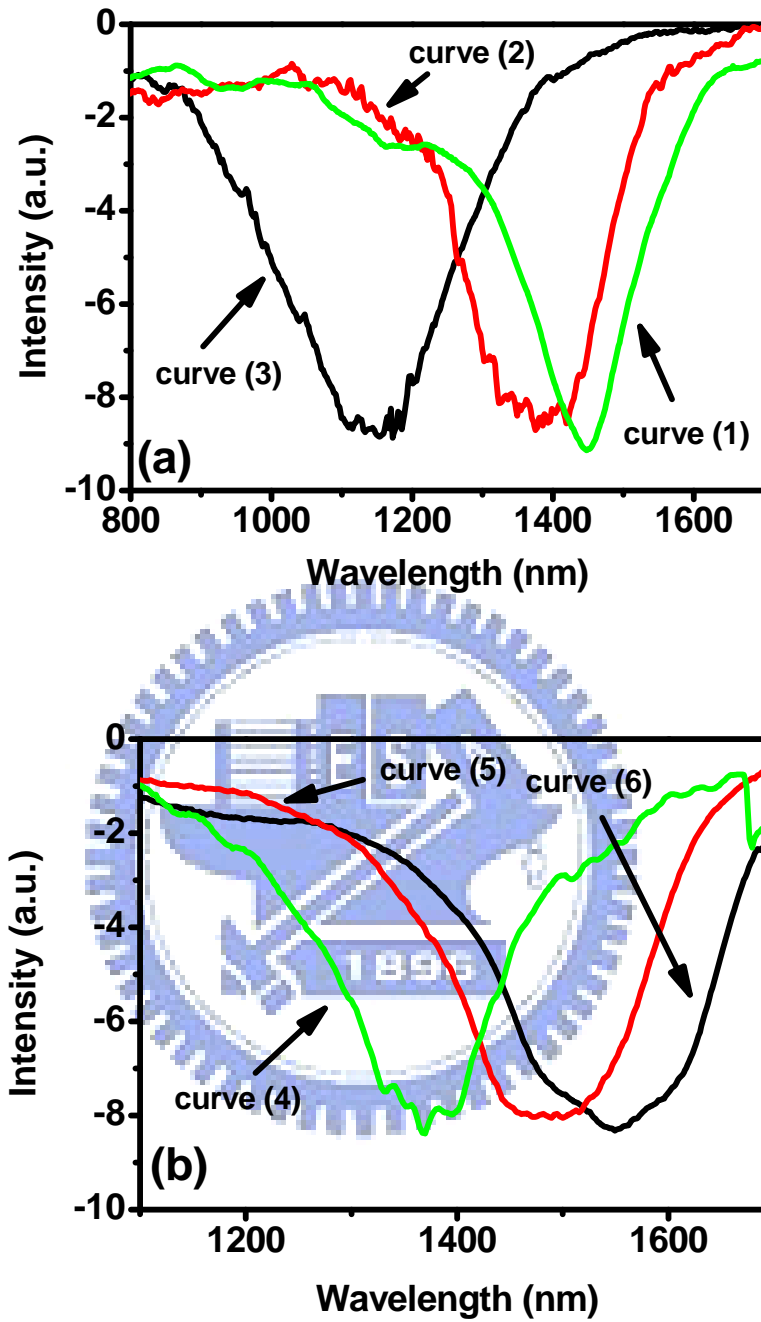


Fig. 4-4. Transmission spectra for (a) Chirped single-LPG, (b) Chirped single-LPG by rotating 90 degrees of the V-grooved metallic plate.

### 4.1.3 Polarization dependence of LPG



The setup of measurement is similar with that Fig. 3-4 (a) except that a polarizer and a polarization controller are added and connected with the unpolarized white light source. The input signal was firstly launched through the polarizer and then followed by the polarization controller. The length of LPG used for polarization measurements was about 2 cm and its effective period,  $\Lambda_{\text{eff}}$ , was equal to 573  $\mu\text{m}$ .

Fig. 4-5 shows the transmission loss spectra around the 1190 nm peak of the LPG in the ESM-12-01 fiber, taken with polarized light and corresponding to the maximum [curve (1)] and minimum [curve (2)] amplitude of the transmitted signal. The input angles for the maximum and minimum amplitude spectra differ by 90 degree, thus corresponding well to LPGs mechanically induced in photonic crystal fiber [1].

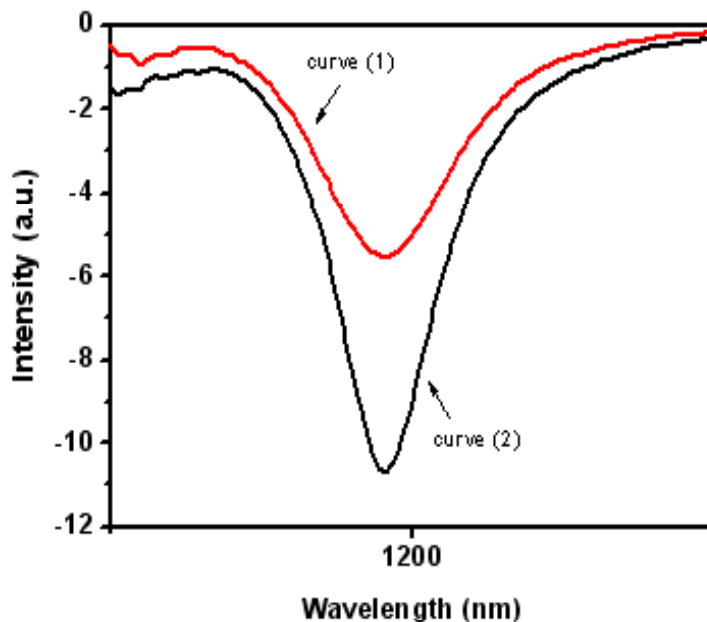


Fig. 4-5 Transmission spectra for LPG in PCF taken with polarized light and corresponding to maximum and minimum amplitudes of transmitted power

#### 4.1.4 Generation and elimination of spectrum fringes

The single-LPG can be generated in a bended PCF by pressing the PCF as in Fig. 3-4(c). Transmission spectra for the chirped single-LPGs are shown in Fig. 4-6, and the modulation depth increases with increasing pressure as shown in Fig. 4-7. The ultra-broad transmission bandwidths should be attributed to the varying periodicity along the chirped PCF-LPGs. We find that chirped single LPG would show spectral fringes [curve (i)] and the fringe spacing could be uneven, depending on the interaction length and chirping level between the two ends of the LPG. For curve (i), the wavelength spacing between adjacent fringe peaks is uneven, ranging from 43 nm to 110 nm. With chirped single-LPG configuration of increased chirping level, we find that the spectral fringes will disappear in the rejection band [curve (ii)]. Therefore, chirped single-LPG can be fabricated by the configuration of Fig. 3-4(c) to generate or eliminate the modulation peaks.

Two chirped LPGs can be induced simultaneously by pressing two separate parts of the bended PCF, as by using the configuration of Fig. 3-4(d). Transmission spectra for the chirped dual-LPGs are shown in Fig. 4-8. For the dual-LPG in symmetrically bended PCF, the rejection bandwidth is about 250 nm. As long as the separation between the two induced LPGs is small enough, spectral fringes appear in the rejection band [curve (iii)]. The wavelength spacing between adjacent peaks is about 12.5 nm. On the contrary, when the separation between the two induced LPGs is large enough, spectral fringes are not obvious in

the rejection band [curve (iv)].

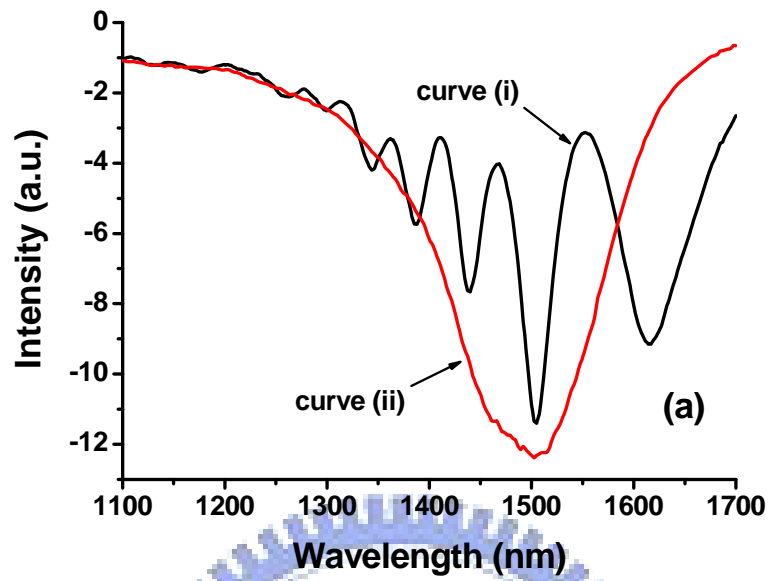


Fig. 4-6. Transmission spectra for spectral fringes can be obtained from chirped single-LPGs, and the fringes can be eliminated with proper configuration.

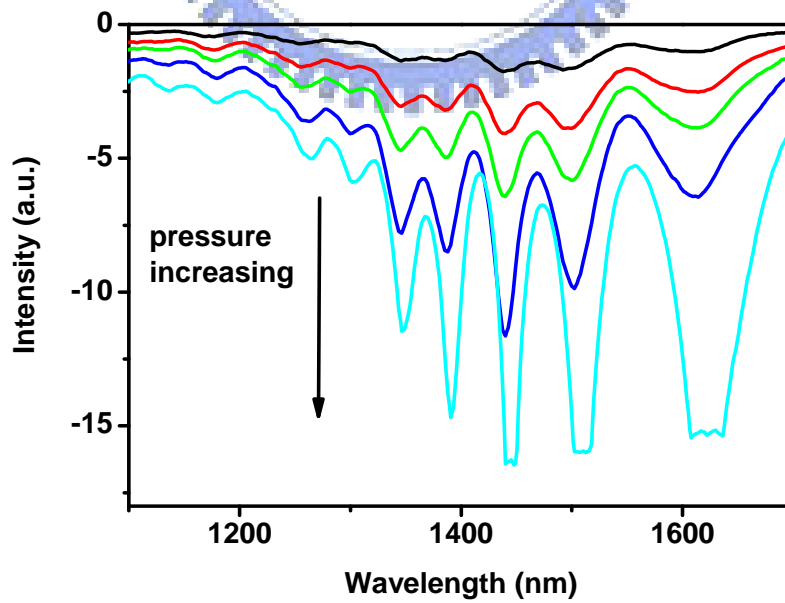


Fig. 4-7. Transmission spectra for spectral fringes with different pressures.

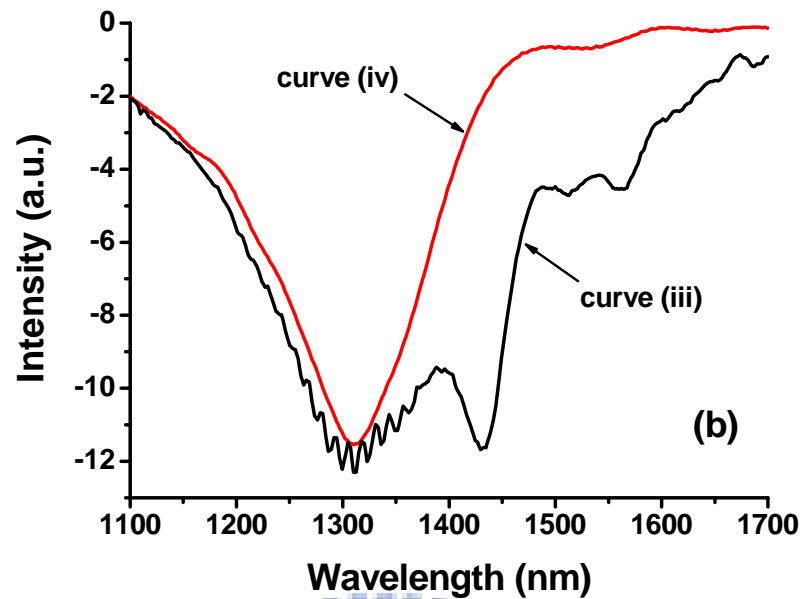


Fig. 4-8. Transmission spectra for spectral fringes can be obtained from chirped dual-LPGs, and the fringes can be eliminated with proper configuration

## 4.2 Transmission spectra of LPGs made by metallic post

### 4.2.1 Chirped LPGs

Another method to induce two chirped LPGs simultaneously is using a wired post. The chirped LPGs are pressed by a corrugated device made by wrapping a long copper wire on a cylindrical metallic post as shown in Fig. 4-9. Transmission spectra for the chirped dual-LPG are shown in Fig. 4-10. The results in Fig. 4-10 are obtained for bended PCF of different curvatures: curve (1) < curve (2) < curve (3). The ultra-broad transmission bandwidth should be attributed to the varying periodicity along the chirped PCF-LPG. We have observed that when the curvature of PCF bending increases, the amount of chirping will increase, leading to the broadening of stop band in the transmission spectra. As shown in

Fig 4-10, spectral modulation fringes are observed in the rejection band, and the modulation depth increases with the amount of chirping. The spectrum fringes should be MZ interference. The rejection bandwidth is changed from 79 nm to 300 nm, and the fringe spacing is about 18 nm.

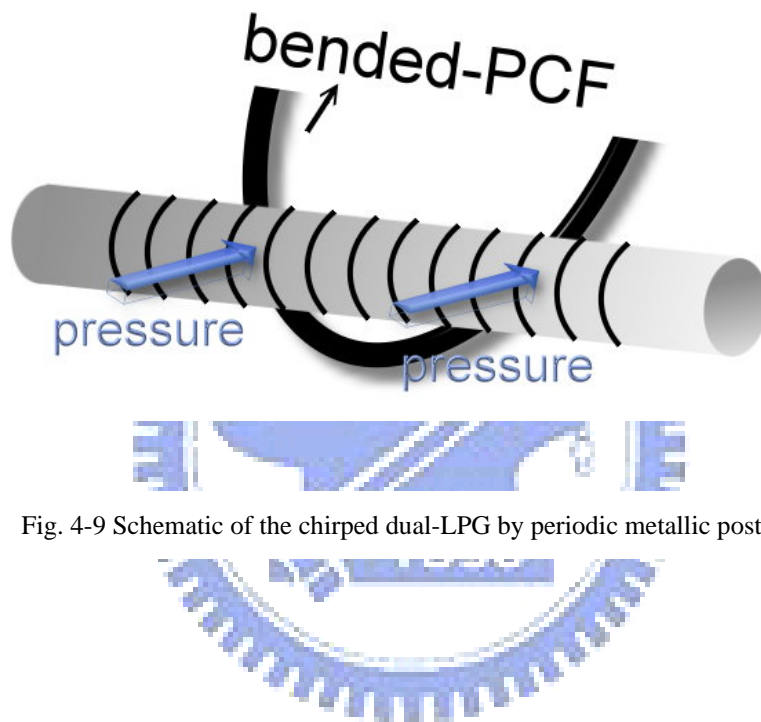


Fig. 4-9 Schematic of the chirped dual-LPG by periodic metallic post

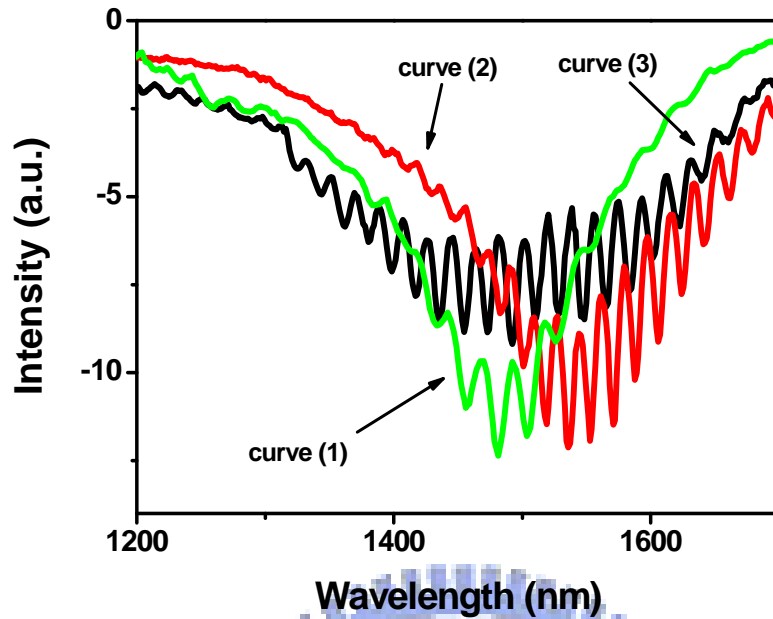
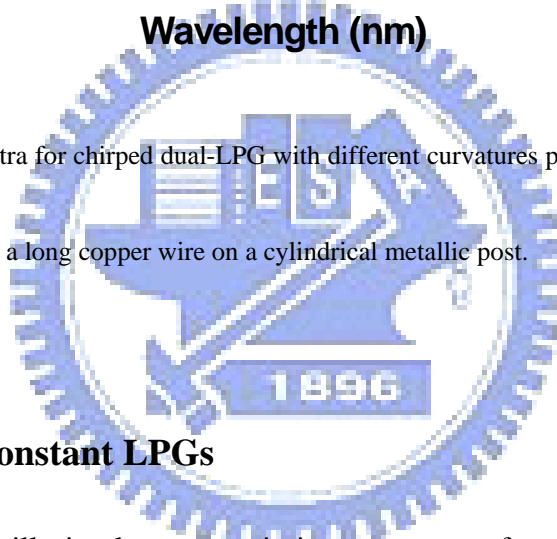


Fig. 4-10. Transmission spectra for chirped dual-LPG with different curvatures pressed by a corrugated device made by wrapping a long copper wire on a cylindrical metallic post.



### 4.3 Simulation of constant LPGs

In the section, I will simulate transmission spectrum of constant-period LPGs. The effective index of different modes can be obtained by using R-soft software (Rsoft Design Group, Inc.). The cross section of PCF layout through R-soft software as shown in Fig. 4-11, and the parameter of ESM-12-01 is pitch  $\sim 8 \mu\text{m}$ , filling factor  $\sim 0.46$ , core diameter  $\sim 12 \mu\text{m}$ , cladding diameter  $\sim 128 \mu\text{m}$ .

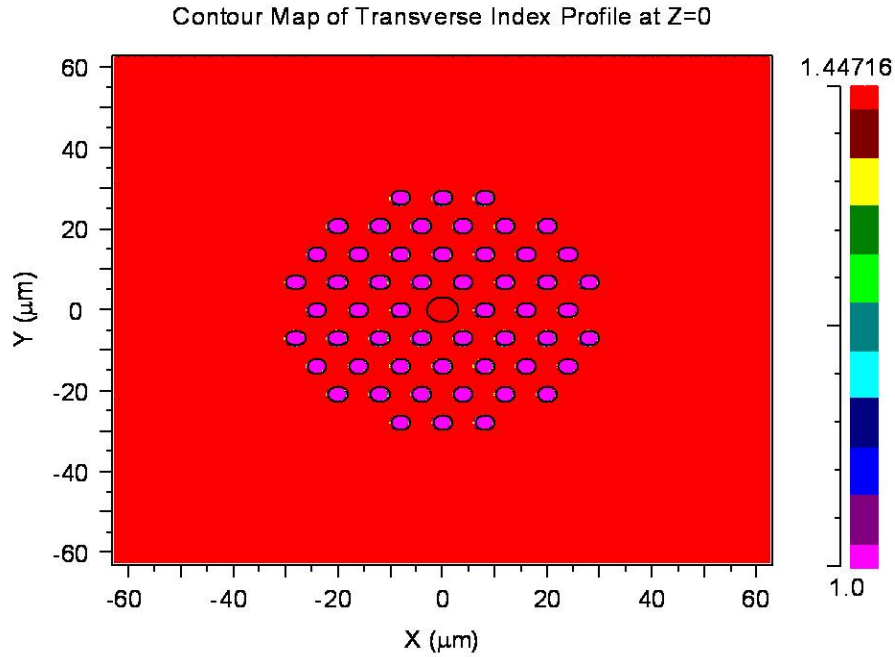


Fig. 4-11. The cross section of PCF appear in the CAD windows.

Because cladding parts of the PCF is highly pure fused-silica, so we use Sellmeier equation to calculate material dispersion as in Eq. (4.3-1), and the coefficients of Sellmeier equation used for highly pure fused-silica fiber are shown in table 4-1. The material dispersion is shown in Fig. 4-12.

$$n^2(\lambda) = 1 + \frac{G_1 \times \lambda^2}{\lambda^2 - \lambda_1^2} + \frac{G_2 \times \lambda^2}{\lambda^2 - \lambda_2^2} + \frac{G_3 \times \lambda^2}{\lambda^2 - \lambda_3^2} \quad (4.3-1)$$

Table 4-1. The coefficient of Sellmeier equation used in highly pure fused-silica fiber.

$G_1$	0.6965325
$G_2$	0.4083099
$G_3$	0.8968766
$\lambda_1$	0.066 $\mu\text{m}$
$\lambda_2$	0.118 $\mu\text{m}$
$\lambda_3$	9.896 $\mu\text{m}$

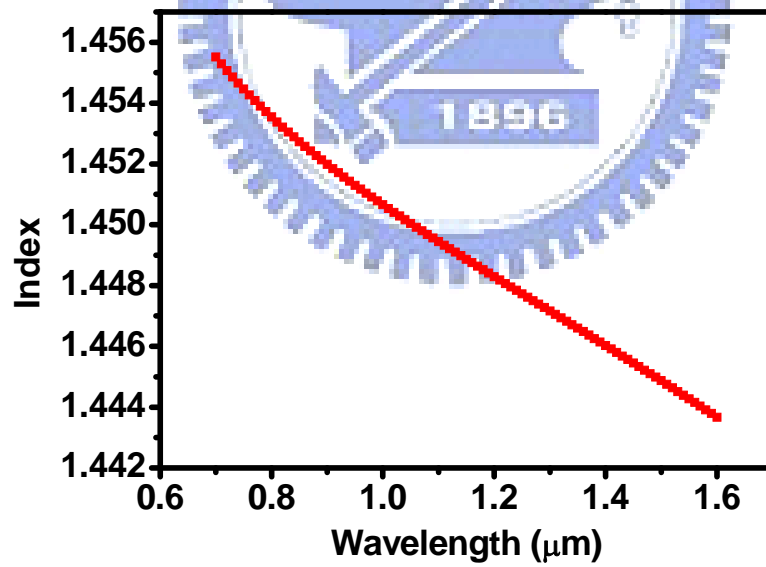


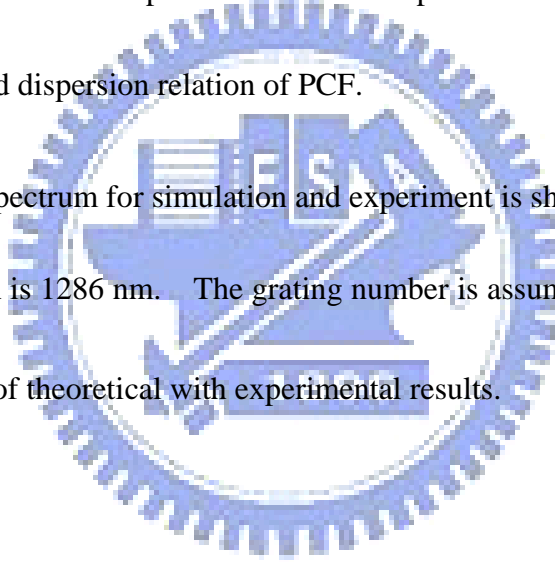
Fig. 4-12. Material dispersion of the highly pure fused-silica fiber.



After calculating the material dispersion, we substitute it into R-soft software. We launched a Gaussian pulse which has different incident position to excite the guiding mode and different cladding mode by correlation method of beam propagation method in PCF. The step size of BMP is  $0.3 \mu\text{m}$ , and length of simulation is  $2^{17}$  multiplied by  $0.3$ . The dispersion relation of PCF is shown in Fig. 4-13, where  $m_0$  is fundamental core mode and  $m_1 \sim m_3$  is the higher order cladding modes.

Finally, we got transmission spectrum of constant period LPGs by using coupled-mode theory [Eq. (2.2-16)] and dispersion relation of PCF.

The transmission spectrum for simulation and experiment is shown in Fig. 4-14, where the resonant wavelength is  $1286 \text{ nm}$ . The grating number is assumed to be 50, and  $\kappa L = \frac{3\pi}{4}$ . It is in good agreement of theoretical with experimental results.



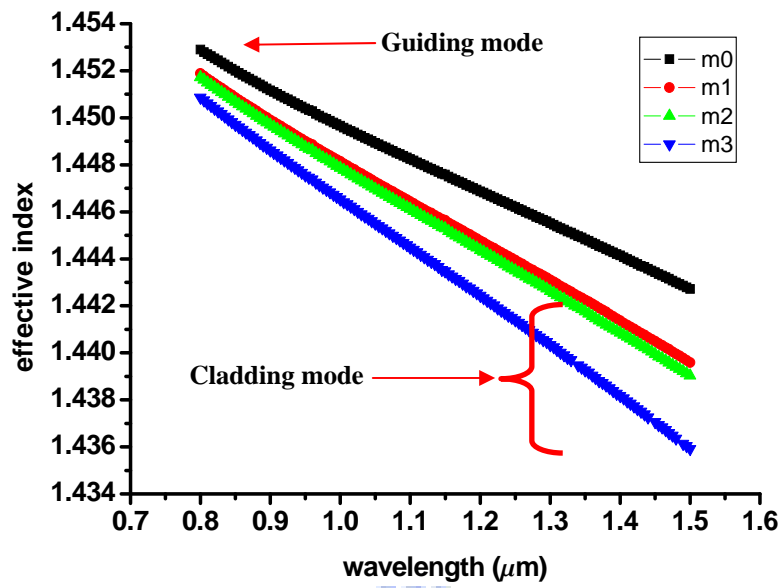


Fig. 4-13. The effective index of core mode and high order cladding mode are found in

PCF;  $m_0$ : fundamental core mode,  $m_1 \sim m_3$ : high order cladding modes.

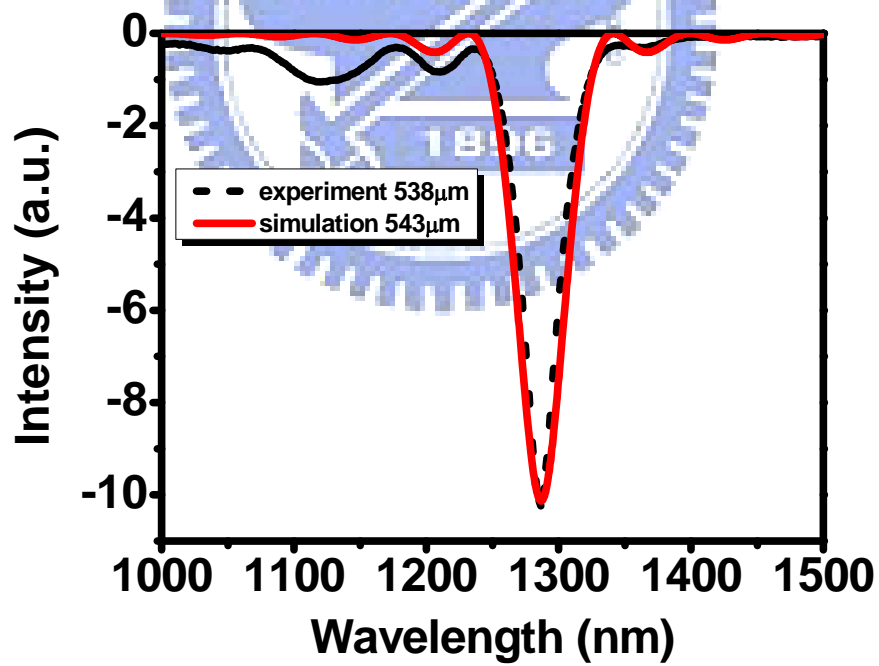
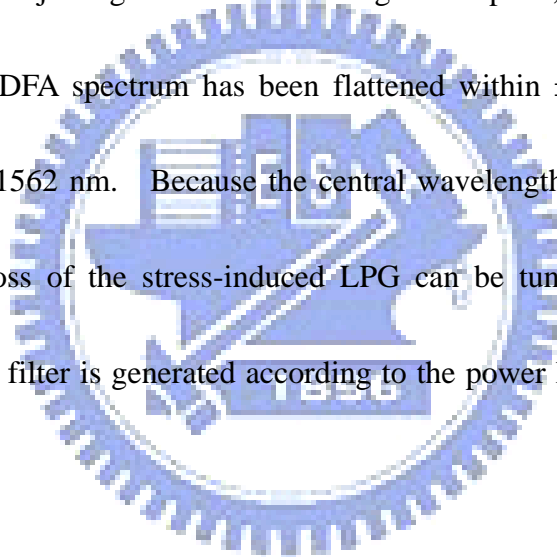


Fig. 4-14. Transmission spectrum for simulation and experiment, and resonant wavelength is 1286 nm.

## 4.4 Application

### 4.4.1 Gain flattening of Erbium-Doped Fiber Amplifier

As an application, we have used the stress-induced LPG in the gain flattening of erbium-doped fiber amplifier. Insets of Fig. 4-15 show the original EDFA output spectrum and the flattening result, with EDFA pump current of 28 mA. The amplified spontaneous emission (ASE) spectrum of EDFA shows a peak around 1532 nm. By cascading a PCF-LPG and carefully adjusting the direction of V-grooved plate, the PCF bending, and the mechanical pressure, EDFA spectrum has been flattened within  $\pm 1$  dB for spectral range between 1528 nm and 1562 nm. Because the central wavelength, the rejection bandwidth, and the transmission loss of the stress-induced LPG can be tuned over a broad range, a versatile gain-flattening filter is generated according to the power level and spectral range of the EDFA.



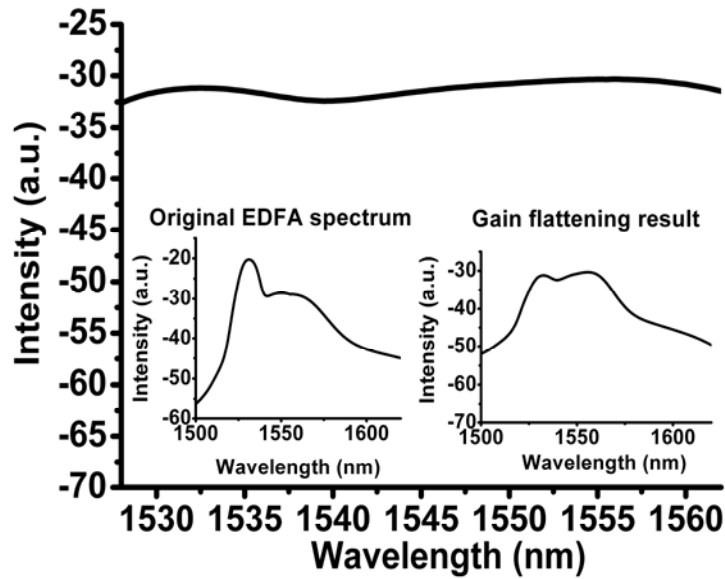


Fig. 4-15 The gain flattened EDFA spectrum between 1528 nm and 1562 nm by using the chirped LPGs.

Insets are original EDFA spectrum and gain flattening result, the pump current of the EDFA is 28mA.

## 4.5 Summary

In the section, we investigate a method for generating versatile tunable long-period gratings (LPGs) in photonic crystal fibers (PCFs) by using two kinds of corrugated devices.

As the chirping increases, the rejection bandwidth in the transmission spectra of long-period fiber gratings increases. However, the effective periodicity increases with increased chirping, and the center wavelength of rejection band decreases. On the contrary, the effective periodicity decreases as the chirping increases, and thus the center wavelength of rejection band increases with increased bending. The 3-dB bandwidth of chirped dual-LPG and single-LPG can be tuned from 70 nm to 300 nm. For constant period LPG, the resonant wavelength can be tuned over 800 nm spectral range, and the 3-dB bandwidth is changed from 10 nm to 50 nm. Spectral fringes with uneven spacing are observed in chirped LPGs,

depending on the interaction length and the amount of chirping between the two ends of the LPG, and can be removed by reducing interaction length and chirping. By using proper configurations, we can fabricate PCF-LPGs to either generate or eliminate the modulation peaks. By utilizing a stress-induced LPG, gain flattening of an erbium-doped fiber amplifier has also been demonstrated.



## References

- [1] J. H. Lim, K. S. Lee, J. C. Kim, and B. H. Lee, "Tunable fiber gratings fabricated in photonic crystal fiber by use of mechanical pressure," *Opt. Lett.* **29**, 331-333 (2004).



# Chapter 5 Supercontinuum generation using Q-switched mode-locking Nd<sup>3+</sup>:GdVO<sub>4</sub> laser with Cr<sup>4+</sup>:YAG saturable absorber

## 5.1 Q-switched mode-locked Nd<sup>3+</sup>:GdVO<sub>4</sub> laser with Cr<sup>4+</sup>:YAG saturable absorber

The output power versus the wavelength at the CW states (black squares) as well as the QML states generated by the Cr<sup>4+</sup>:YAG, with various initial transmissions of the saturable absorber  $T_0=80\%$  (red diamonds), 55% (green triangles) and 40% (blue circles) are shown in Fig. 5-1. By comparing the threshold of  $T_0=80\%$ ,  $T_0=55\%$ , and  $T_0=40\%$ , we found that the laser threshold pump powers increase with increased initial transmittance of Cr<sup>4+</sup>:YAG. The laser threshold pump power is 3.5 W for  $T_0=80\%$ , 7 W for  $T_0=55\%$ , and 10.5 W for  $T_0=40\%$ .

The oscilloscope traces of pulse trains of QML are shown in Fig. 5-2. There are vivid differences below: irregular pulse train with large fluctuation is observed for 80% Cr<sup>4+</sup>:YAG but rather stable with small fluctuation for 40% Cr<sup>4+</sup>:YAG.

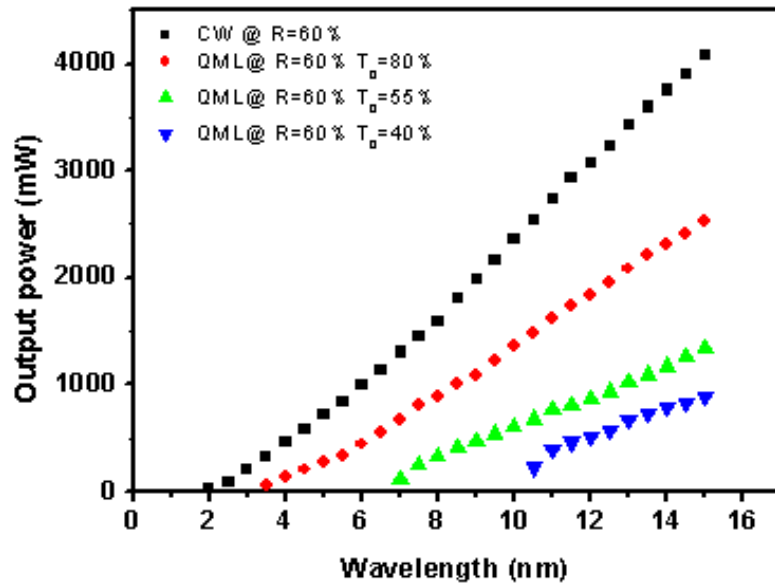


Fig. 5-1 The average power versus pump power at CW state (black squares), as well as QML states with  $T_0 = 80\%$  (red diamonds),  $55\%$  (green triangles), and  $40\%$  (blue triangles).

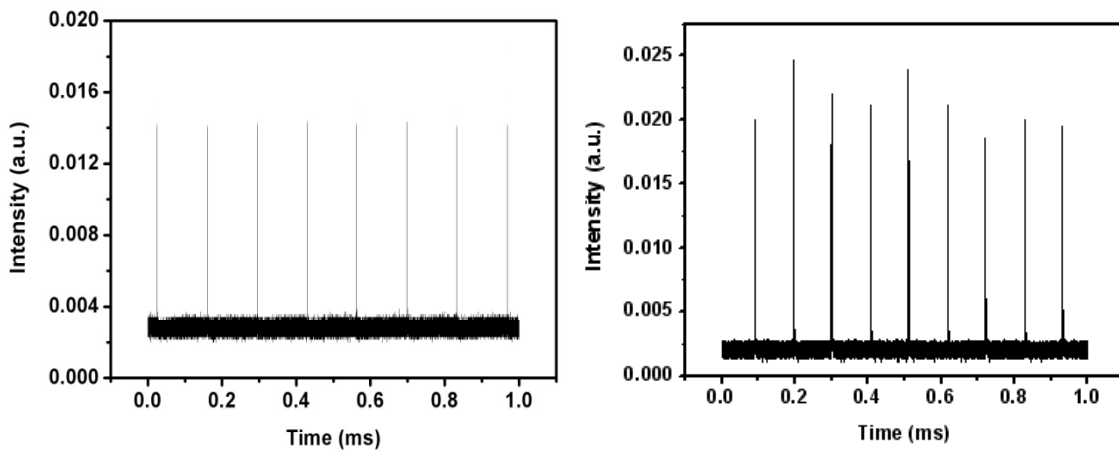


Fig. 5-2 Pulse train of QML with  $T_0 = 40\%$  (Left), and  $T_0 = 80\%$  (Right)

The expanded Q-switching envelopes containing multiple mode-locked (ML) pulses were shown in Fig. 5-3~5-5, where the laser was pumped at 12 W with the OC reflectivity of,



R=60%, and the transmittance of Cr<sup>4+</sup>:YAG is T<sub>0</sub> = 80% ( Fig.5-3 ), 55% ( Fig.5-4 ), and 40% ( Fig.5-5 ). The discrete ML pulses with time interval of ~ 8 ns can be obviously seen inside the Q-switched envelope. By fitting the envelope with the formula:

$$Intensity = \left\{ \frac{a}{\exp[(1.76 * t / t_1] + \exp[-1.76 * t / t_2]} \right\}^2 \quad (5.1-1)$$

where t<sub>1</sub> is the rising time and t<sub>2</sub> is the falling time, the width and symmetric factor of the Q-switched envelope can be estimated by (t<sub>1</sub>+t<sub>2</sub>)/2 and t<sub>1</sub>/t<sub>2</sub>. The width of the Q-switched envelope increases as T<sub>0</sub> increases. For instance, the width of the Q-switched envelope is about 56 ns for T<sub>0</sub> = 40% and 74 ns for T<sub>0</sub> = 55%, whereas the width becomes 169 ns for T<sub>0</sub> = 80%.

The shape of envelope will become more symmetric as the ratio of initial population inversion (n<sub>i</sub>) before the Q-switch open to the population inversion at threshold (n) increases.

The initial inversion n<sub>i</sub> can be obtain by the formula:

$$n_i = \frac{\ln(1/T_0^2) + \ln(1/R) + L}{2\sigma l} \quad (5.1-2)$$

where L is nonsaturable intracavity round-trip dissipative optical loss, and σ is stimulated emission cross section of the gain medium. From the formula, the shape of envelope will become more symmetric at higher T<sub>0</sub> for the same output coupler, which can be observed in Fig.5-3~5-5. In the Fig. 5-3~5-5., the ratio is the modulation depth of Q-switched mode-locking. We define the ratio as the highest trough value to the modulation value. For the same output coupler, the ratio increases when T<sub>0</sub> increases, as shown in Fig. 5-3~5-5.

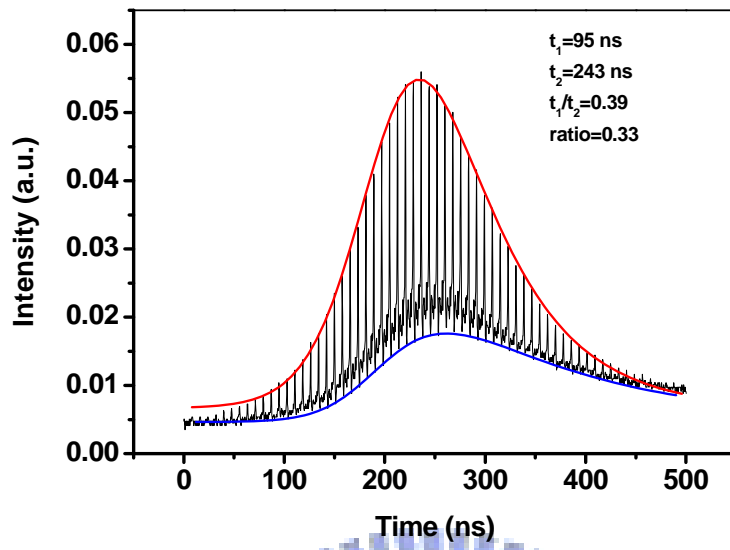


Fig. 5-3 Temporal expansion of Q-switching envelope of 80% Cr<sup>4+</sup>:YAG with fitting in red

line and blue line

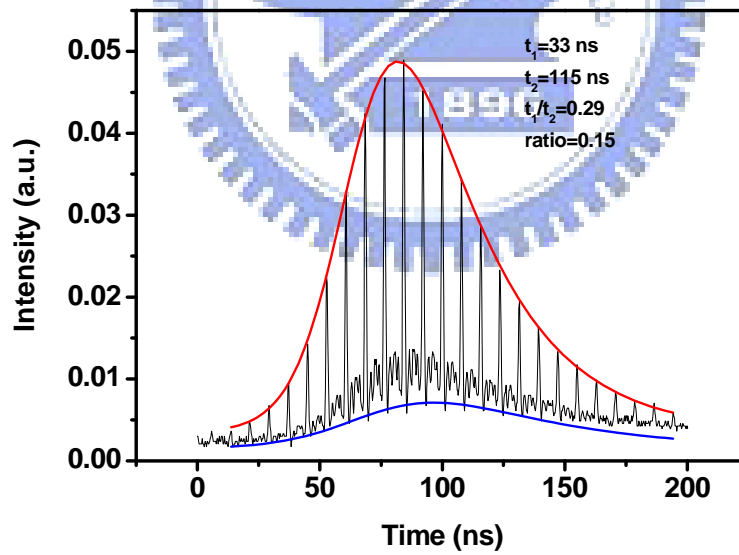


Fig. 5-4 Temporal expansion of Q-switching envelope of 55% Cr<sup>4+</sup>:YAG with fitting in red line and

blue line.

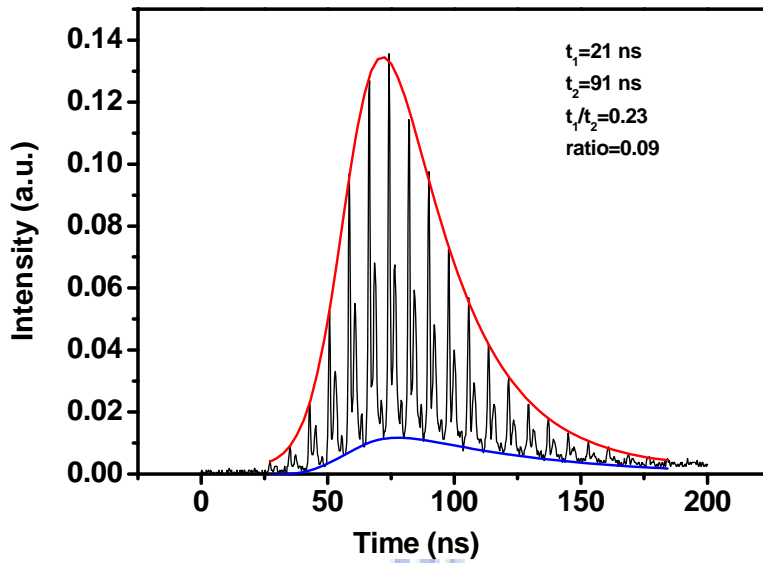
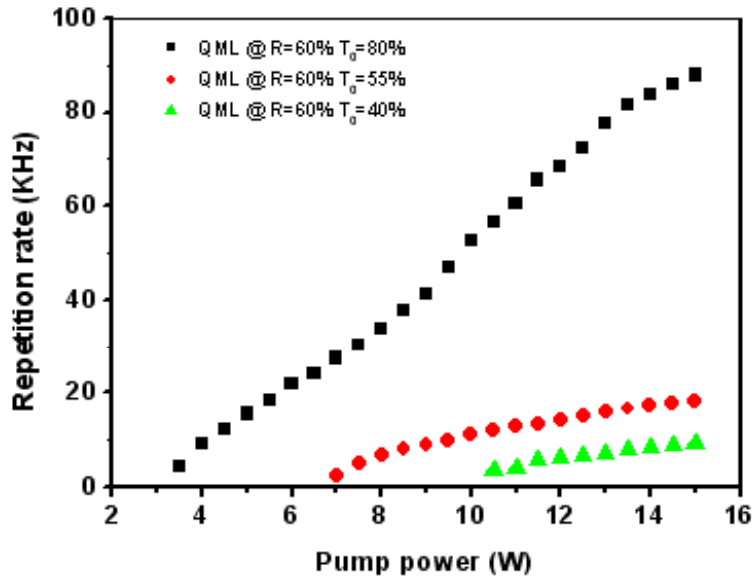


Fig. 5-5 Temporal expansion of Q-switching envelope of 40% Cr<sup>4+</sup>:YAG with fitting in red line and blue line

The measured repetition rates ( $R_{ep}$ ) in Fig. 5-6 show the increase tendency as the pump powers increase. For  $T_0=80\%$ ,  $R_{ep}$  reveals obviously and linearly increases as  $P_p$  increase. However, the slope efficiency of the repetition rate  $R_{ep}$  for  $T_0 = 55\%$  and  $40\%$  is smaller. The highest repetition rate is about 87 kHz for  $T_0 = 80\%$  that is relatively higher than the 18 kHz and 9 kHz for  $T_0 = 55\%$  and  $40\%$ , respectively.



Fig, 5-6 Repetition rates versus the pump power at the QML states with the  $T_0=80\%$

(black squares), 55% (red diamonds), and 40% (green triangles).

Our central goal is to produce a high peak power and high pulse energy laser, which will be launched into photonic crystal fiber to generate supercontinuum spectrum. Fig. 5-7 shows the estimated pulse energy versus the pump power for the QML states at different  $T_0$  values by using the formula:

$$E_p = \frac{P_{av}}{R} \tag{5.1-2}$$

The pulse energy increases as  $T_0$  decreases due to apparently decrease of the repetition rate, and the highest pulse energies can be obtained at 15 W pumped power about 96  $\mu\text{J}$  for  $R = 60\%$  and  $T_0 = 40\%$ . Our Q-switched mode-locking Nd:GdVO<sub>4</sub> laser has achieved a repetition rate of 9 kHz, highest output power of 1 W, and pulse energy of 96  $\mu\text{J}$ . Thus, efficient white light supercontinuum generation will become possible.

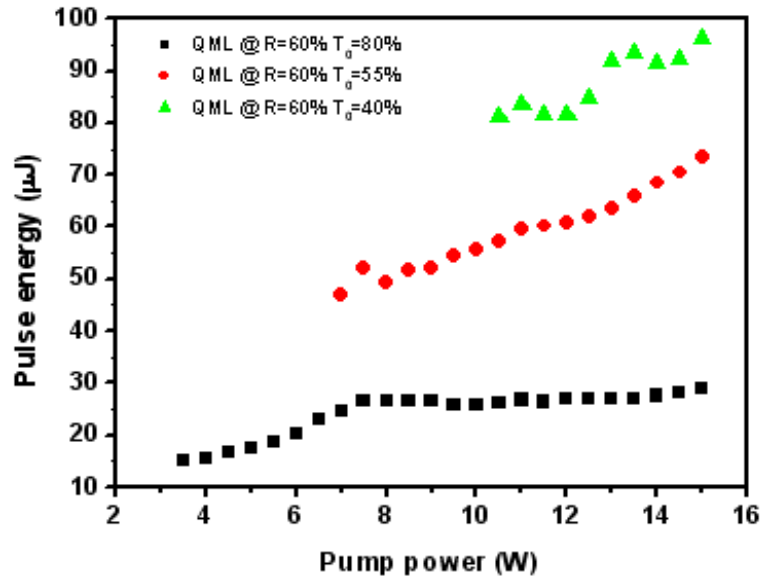


Fig. 5-7 The estimated pulse energy versus the pump power at the QML states with  $T_0=80\%$  (black squares), 55% (red diamonds), and 40% (green triangles)

## 5.2 Simulation of Q-switched mode-locking

We use the rate equations containing the cavity photon density in the gain medium and absorber population to simulate the QML envelope. The output power of the laser can be expressed in term of the photon density using equation (2.2-14). By simulating equation (2.2-12), we get the similar result seen on the oscilloscope as shown in Fig. 5-8~5-10.

The key point is that 40% has fewer mode-locked pulses in Q-switch envelope than 55% and 80%. By using the simulation, we can predict the result of various kinds of reflections versus transmission of Cr:YAG. However, too high reflection will not provide enough modulation depth for mode-locking pulses and therefore it's just like that the mode-locked pulses are added on an AC value shown in Fig 5.3 where it wipes out the bottom part of Q-switching envelope.

In the following simulations we only alter the transmission of Cr:YAG and fix the output coupler at  $R = 60\%$ . The time expansion of one QML envelope for  $T_0$  varying from 40% to 80% is shown in Fig. 5-8~5-10.

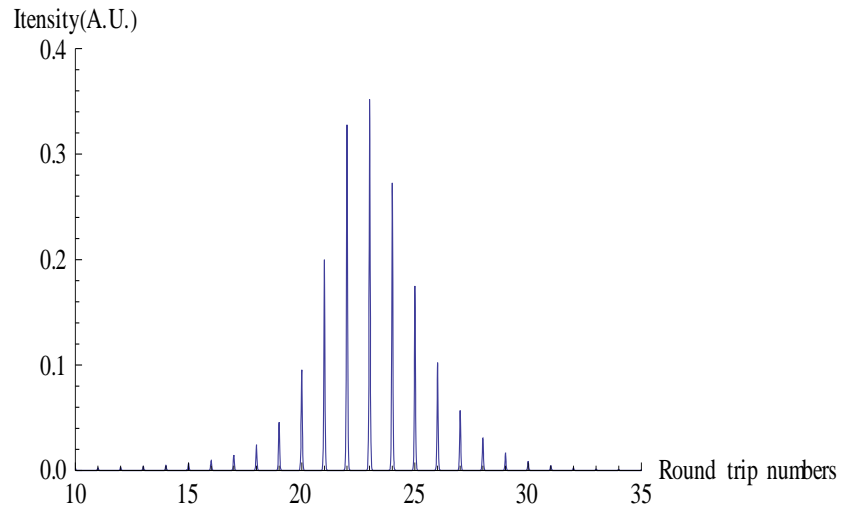


Fig. 5-8 Calculated result for the temporal shape of a single Q-switched envelope for saturable absorbers of  $T=40\%$  with  $R=60\%$

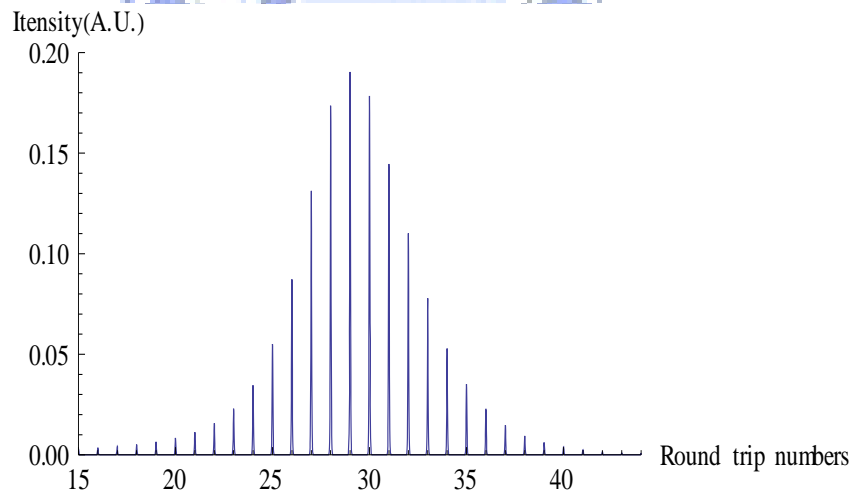


Fig. 5-9 Calculated result for the temporal shape of a single Q-switched envelope for saturable absorbers of  $T=55\%$  with  $R=60\%$ .

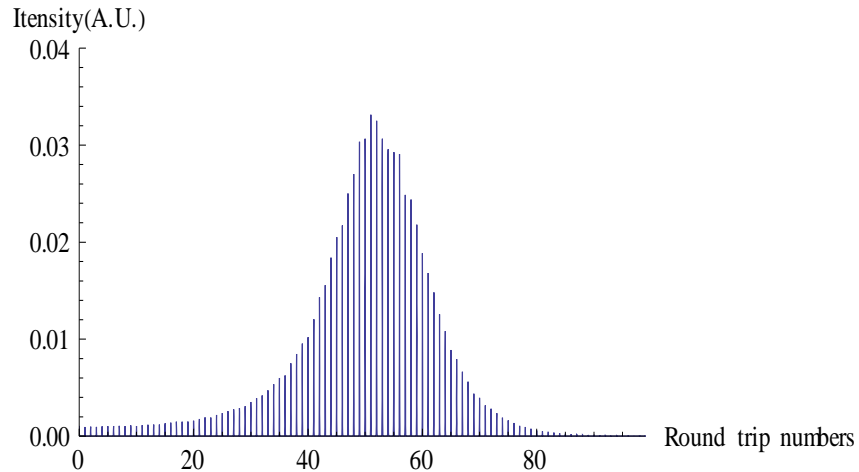


Fig. 5-10 Calculated result for the temporal shape of a single Q-switched envelope

for saturable absorbers of  $T=80\%$  with  $R=60\%$ .

As can be observed in Fig. 5-8~5-10, more pulses is produced inside the envelope with higher transmission of Cr:YAG. The strong evidence of Fig 5.8~5-10 also convinces us that lower transmission could perform a better result for the QML, however, the higher threshold has to pay for penalty.

### 5.3 Supercontinuum generation by QML laser using PCFs

Effective supercontinuum (SC) generation is demonstrated by injecting picosecond Q-switched mode-locked Nd:GdVO<sub>4</sub> laser pulses into a 1-m long microstructured fiber. The laser is operated at wavelength 100-nm away from the longer zero-dispersion of this dual zero-dispersion wavelength microstructured fiber. The phenomena of modulation instability, stimulated Raman effect, and dispersive wave can be sequentially observed from experimental results, leading to spectral broadening as pumping increases.

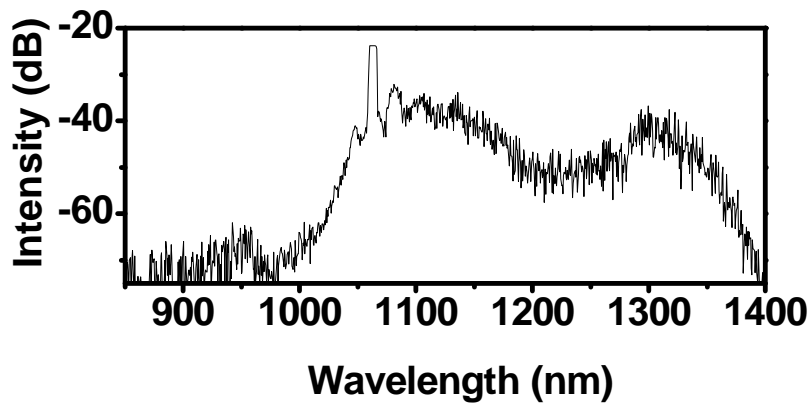


Fig. 5-11 The evolutions of spectral broadening for the experimental observation as pumping power increases.

## 5.4 Summary

We have demonstrated the Q-switched and mode-locked operation of the Nd:GdVO<sub>4</sub> laser in use of the Cr<sup>4+</sup>:YAG as the saturable absorber. The obtained shape of Q-switched envelope, repetition rate and pulse energy are demonstrated to depend on the initial transmittance of the Cr<sup>4+</sup>:YAG. Using  $R = 60\%$  and  $T_0 = 40\%$ , the highest pulse energy of 96  $\mu\text{J}$  of each Q-switched envelope can be obtained at 15 W pump power. We use the rate equations containing the cavity photon density in the gain medium and absorber population to simulate the QML envelope. Picosecond Q-switched mode-locked pulses can be produced at lower pump power from Nd:GdVO<sub>4</sub> laser. Due to lower repetition rate and higher peak power of Q-switched mode-locked pulses than CW mode-locked pulses at the same average power, the QML pulses can be used to effectively generate supercontinuum in microstructured fiber as short as only 1 m.



## Chapter 6 Conclusions and future works

In the thesis, we have investigated two topics: (1) generation of versatile tunable long-period gratings in photonic crystal fibers, and (2) study of Q-switched and mode-locked operation in a diode-pumped Nd:GdVO<sub>4</sub> laser by using different initial transmittance of Cr<sup>4+</sup>:YAG crystal.

First, we report a method for generating versatile tunable long-period gratings (LPGs) in photonic crystal fibers (PCFs) by using two kind of corrugated devices. As the chirping increases, the rejection bandwidth in the transmission spectra of long period fiber gratings increases. However, the effective periodicity increases with increased chirping, and the center wavelength of rejection band decreases. On the contrary, the effective periodicity decreases as the chirping increases, and thus the center wavelength of rejection band increases with increased bending. The 3-dB bandwidth of chirped dual-LPG and single-LPG can be tuned from 70 nm to 300 nm. For constant period LPG, the resonant wavelength can be tuned over 800 nm spectral range, and the 3-dB bandwidth is changed from 10 nm to 50 nm. Spectral fringes with uneven spacing are observed in chirped LPGs, depending on the interaction length and the amount of chirping between the two ends of the LPG, and can be removed by reducing interaction length and chirping. We also used beam propagation method and coupled-mode theory to simulate the transmission spectrum of constant period LPG, and it is in good agreement with experimental results. By utilizing a stress-induced

LPG, gain flattening of an erbium-doped fiber amplifier has also been demonstrated.

Second, We investigate the Q-switched and mode-locked operation in a diode-pumped Nd:GdVO<sub>4</sub> laser by using different initial transmittance  $T_0$  of Cr<sup>4+</sup>:YAG crystal. The highest pulse energy of Q-switched envelope about 96  $\mu$ J can be obtained at 15 W pump power. Finally, supercontinuum is generated by using a Q-switched mode-locked laser coupling to a nonlinear photonic crystal fiber.

There are still many works need to be accomplished in the future. I will continue to investigate chirped PCF-LPGs and other PCF-related devices both experimentally and theoretically, in which the chirped LPG will be simulated by coupled mode theory and finite element method. In addition, supercontinuum can be easily generated by using our last case. Furthermore, the high peak power excitation is convenient for stimulating the carriers in photonic materials and low repetition rate is also essential for preventing thermal heating effect. Therefore, the light source built here is quite suitable for material characterizations such as Z-scan and pump-probe spectroscopy.